

High-resolution, energy-dispersive microcalorimeter spectrometer for X-ray microanalysis

D. A. WOLLMAN,* K. D. IRWIN,* G. C. HILTON,* L. L. DULCIE,* D. E. NEWBURY† & J. M. MARTINIS*

*National Institute of Standards and Technology (NIST), Boulder, CO 80303, U.S.A.

†National Institute of Standards and Technology (NIST), Gaithersburg, MD 20899, U.S.A.

Key words. Count rate, EDS, energy-dispersive detector, high energy resolution, microcalorimeter spectrometer, microcalorimeter, particle identification, polycapillary X-ray optics, solid angle, TES microcalorimeter, WDS, X-ray microanalysis, X-ray microcalorimeter, X-ray spectroscopy.

Summary

We have developed a prototype X-ray microcalorimeter spectrometer with high energy resolution for use in X-ray microanalysis. The microcalorimeter spectrometer system consists of a superconducting transition-edge sensor X-ray microcalorimeter cooled to an operating temperature near 100 mK by a compact adiabatic demagnetization refrigerator, a superconducting quantum interference device current amplifier followed by pulse-shaping amplifiers and pileup rejection circuitry, and a multichannel analyser with computer interface for the real-time acquisition of X-ray spectra. With the spectrometer mounted on a scanning electron microscope, we have achieved an instrument response energy resolution of better than 10 eV full width at half-maximum (FWHM) over a broad energy range at real-time output count rates up to 150 s^{-1} . Careful analysis of digitized X-ray pulses yields an instrument-response energy resolution of $7.2 \pm 0.4\text{ eV}$ FWHM at 5.89 keV for Mn $K\alpha_{1,2}$ X-rays from a radioactive ^{55}Fe source, the best reported energy resolution for any energy-dispersive detector.

Introduction

X-ray spectroscopy is one of the most sensitive, nondestructive analytical techniques for chemical analysis, providing both qualitative and quantitative compositional information. The integration of high-energy-resolution X-ray spectrometers with high-spatial-resolution electron microscopes has led to powerful and widely used microanalysis instruments. A finely focused electron beam is used to excite characteristic X-rays, making it possible to identify and quantify the elemental composition of a sample on a

micrometre or even a nanometre length scale. This analytical capability is essential to modern technology-intensive industries, such as the semiconductor industry. With features of interest for microanalysis continually shrinking to sizes significantly below $1\text{ }\mu\text{m}$, new generations of microanalysis instruments are required to meet the materials analysis challenges of the future.

Two types of X-ray spectrometers are currently used for X-ray microanalysis, wavelength-dispersive (WD) and energy-dispersive (ED) spectrometers. Wavelength-dispersive spectrometers (WDS) have been used since the introduction of the first electron microprobe (Castaing, 1951). In a WDS system, an X-ray wavelength is selected for measurement by mechanically adjusting the incident angle of a curved diffracting crystal to satisfy the Bragg reflection condition. The resulting monochromatic X-rays are then detected with a fast, gas-filled proportional detector. By using a variety of crystals and synthetic multilayers with different layer spacings, it is possible to acquire a complete X-ray spectrum by sequentially scanning over the entire energy range of interest (from about 100 eV to 12 keV). WD spectrometers have low quantum and geometrical collection efficiency but excellent energy resolution, typically 2–20 eV full width at half-maximum (FWHM). Both the efficiency and the energy resolution are strong functions of wavelength and the diffracting crystal. Owing to their mechanical nature, critical geometric requirements and serial operation, WD spectrometers can be slow, difficult to operate and susceptible to systematic errors.

A revolutionary advance in the field of X-ray spectrometry occurred in 1968 with the introduction of the semiconductor ED spectrometer (Fitzgerald *et al.*, 1968). With these new EDS instruments, the rapid simultaneous detection of the entire X-ray energy range (100 eV to over

20 keV for present ED spectrometers) was possible for the first time. ED spectrometers typically use lithium-drifted silicon (Si(Li)) or high-purity germanium (HPGe) solid-state detectors cooled by liquid nitrogen. In these intrinsic semiconductors, the absorption of an X-ray leads to the creation of many electron-hole pairs which separate under an applied voltage bias and are collected on electrodes as a charge pulse. The mean number of electron-hole pairs and thus the total charge collected on the electrode is proportional to the energy of the incident X-ray. A charge-to-voltage preamplifier converts the charge pulse to a voltage step of typically a few millivolts, with a time duration on the order of 10–100 ns. In order to achieve good energy resolution, it is necessary to average over the noise fluctuations on either side of the voltage step. This is done using a pulse-shaping linear amplifier to convert the voltage steps to shaped pulses, suitable for input to a multichannel analyser, with peaking times of up to tens of microseconds and peak heights of 0–10 V.

Semiconductor ED spectrometers have become the spectrometers of choice for most microanalysis instruments because they are easy to use, inexpensive to operate, stable over long times, and offer both rapid qualitative evaluation of chemical composition and accurate quantitative analysis. Their widespread use comes despite their relatively poor energy resolution (typically 130 eV FWHM at Mn K α , as opposed to \approx 20 eV FWHM for WD spectrometers) and resulting poor peak-to-background ratios, which lead to reduced limits of detection (typically a mass fraction of 10^{-3} , as opposed to less than 10^{-4} for WD spectrometers (Goldstein *et al.*, 1992)). The poor energy resolution of semiconductor ED spectrometers is a particular problem in severe peak overlap situations, such as the W M α and Si K α peak overlap for tungsten silicide (WSi₂) and the Ba L α and Ti K α overlap for barium titanate (BaTiO₃), both materials of technological importance.

There is an obvious need for new generations of X-ray spectrometers for microanalysis that combine the excellent energy resolution of WD spectrometers with the parallel energy detection capability of semiconductor ED spectrometers. Recently, high-energy-resolution X-ray microcalorimeter spectrometers for improved EDS X-ray microanalysis have been proposed (Lesyna *et al.*, 1993; Nahum & Martinis, 1995; Silver *et al.*, 1996) and demonstrated (Irwin *et al.*, 1996; Wollman *et al.*, 1996; Silver *et al.*, 1997; Wollman *et al.*, 1997a).

In this paper we characterize the X-ray microcalorimeter spectrometer system developed at NIST for use in X-ray microanalysis. In the first section, we describe the basic operating principles and performance of X-ray microcalorimeters. Here we focus on the optimal energy resolution of our detector, as determined from an analysis of a digitally processed ⁵⁵Fe X-ray spectrum. In the following section, we describe the development of a practical microcalorimeter

spectrometer system incorporating analog signal processing and real-time spectrum acquisition on a scanning electron microscope. The performance of the microcalorimeter spectrometer is fully characterized using test specimens of technological importance. Finally, we consider the relative advantages of microcalorimeter, WD and semiconductor ED spectrometers and examine several important microanalysis problems that can be solved using the microcalorimeter spectrometer.

X-ray microcalorimeters

An X-ray microcalorimeter consists of an X-ray absorber in thermal contact with a thermometer. The energy E of an incident X-ray is converted to heat in the absorber, leading to a temperature rise $\Delta T = E/C$, where C is the combined heat capacity of the absorber and thermometer. A measurement of the temperature rise yields the deposited photon energy. The temperature of the microcalorimeter then returns to the equilibrium temperature with a $1/e$ time constant $\tau_0 = C/G$, where G is the thermal conductance between the absorber and the heat bath.

The energy resolution of a microcalorimeter depends on the thermodynamic fluctuations in its equilibrium energy. The thermodynamic fluctuations in the energy of a thermal mass with heat capacity C have FWHM magnitude $\Delta E_{\text{THERM}} = 2.35\sqrt{(k_B T^2 C)}$, where k_B is Boltzmann's constant and T is the temperature of the mass (Reif, 1965). Low operating temperatures ($T \approx 100$ mK) and heat capacities are necessary to achieve small energy fluctuations and thus good energy resolution. The energy resolution of a microcalorimeter may be expressed as $\Delta E_{\text{FWHM}} = \xi \Delta E_{\text{THERM}}$, where ξ is a dimensionless quality factor determined by a variety of parameters including the sensitivity of the thermometer (Moseley *et al.*, 1984).

The first X-ray microcalorimeters used thermometers based on semiconductor thermistors. Unfortunately, power-dissipation effects in thermistors make them relatively insensitive so that they must be used with ultra-low heat capacity semiconducting or superconducting absorbers. When X-rays are absorbed, the resulting temperature rise causes an increase in the electrical resistance of the thermistor. The thermistor is current biased, and voltage pulses are read out using a silicon junction field effect transistor (JFET) operated at 77 K. Semiconductor-thermistor microcalorimeters have achieved energy resolutions of ≈ 8 eV (McCammon *et al.*, 1991; Silver *et al.*, 1996) for 5.89 keV Mn K $\alpha_{1,2}$ X-rays from a radioactive ⁵⁵Fe source. These devices are operated at $T \approx 70$ mK with heat capacities $C \approx 0.1$ pJ K⁻¹ (McCammon *et al.*, 1991), implying an achieved energy resolution about seven times worse than the thermodynamic energy fluctuations in the sensor ($\xi \approx 7$). Unfortunately, further improvement in the energy resolution of these devices has proven to be difficult.

Trapped charges in semiconducting absorbers and long-lived quasiparticle excitations in superconducting absorbers can lead to statistical variations in the thermalization of the X-ray and thus in the measured energy. Finally, limitations on the power dissipation in semiconductor–thermistor thermometers make them intrinsically slow; the lower limit on their time constant of ≈ 1 ms for operation at 100 mK with optimal resolution (McCammon *et al.*, 1993) may limit their use in materials analysis applications.

The results presented in this work are based on a new type of microcalorimeter (Irwin *et al.*, 1996) using a superconducting transition-edge sensor (TES) thermometer, which is a superconducting film biased within its narrow transition from the normal to the superconducting state. Our TES microcalorimeters have a number of advantages over silicon-thermistor devices. First, the greater sensitivity of TES thermometers compared with semiconductor thermistors makes it possible to build detectors with improved energy resolution using normal-metal absorbers with heat capacities up to two orders of magnitude larger. Secondly, superconducting transition edge sensors have low impedance, which makes them relatively insensitive to microphonic pickup and allows them to be easily read out using superconducting quantum interference device (SQUID) current amplifiers. Thirdly, TES microcalorimeters can be made to self-regulate in temperature with strong negative electrothermal feedback, which leads to simpler operation, faster achievable thermal-response times and improved dynamic range.

Because the transition from the normal to the superconducting state occurs over a very narrow temperature range, a superconducting transition-edge sensor is a much more sensitive thermometer than a semiconductor thermistor. This sensitivity makes it possible to build detectors using large normal-metal absorbers with heat capacities ($C \approx 10$ pJ K $^{-1}$) that are greater than can be used with semiconductor thermistors. Unlike semiconductors and superconductors, normal metals are free of metastable states and thus do not suffer from a degradation of energy resolution due to statistical variations in long-lived athermal excitations (McCammon *et al.*, 1993). Furthermore, in semiconducting and superconducting absorbers, most of the deposited energy goes into excitations in the phonon spectrum, which relaxes to a thermal distribution in a slow and complicated manner. In a normal metal absorber, almost all of the energy goes into excitations in the free electrons, which quickly and efficiently relax to a thermal distribution, allowing better energy resolution and faster detector response (Martinis *et al.*, 1997).

The low impedance of TES thermometers ($R \approx 0.1 \Omega$) provides significant advantages over high-impedance semiconductor thermistors ($R \approx 10$ M Ω). Owing to their low impedance, TES microcalorimeters experience negligible microphonic pickup, which is a major problem with

semiconductor thermistor microcalorimeters. Furthermore, TES microcalorimeters easily impedance-match to SQUID current amplifiers. The use of SQUID amplifiers has many advantages over silicon JFETs in low-temperature applications. They are quieter (effective noise temperatures ≈ 0.1 K as opposed to 1 K for Si JFETs), dissipate far less power (less than 1μ W as opposed to fractions of a milliwatt), and can be operated at lower temperatures and thus closer to the detector (4 K or below as compared with 77 K). We use series-array dc SQUIDs (Welty & Martinis, 1991) which have high bandwidth (≈ 10 MHz) and relatively high voltage output (≈ 5 mV) so that they can be read out with a commercial room temperature operational amplifier.

Another major advantage is that TES microcalorimeters can be made to self-regulate in temperature with strong negative electrothermal feedback, which leads to simpler operation, faster thermal-response times and improved dynamic range (Irwin, 1995). The film is biased with a voltage V , and the current flowing through the film is measured with the SQUID amplifier. The heat bath is then cooled to well below the transition temperature of the film. As the film cools, its resistance R drops and the Joule heating (V^2/R) in the film increases. A stable equilibrium is established when the resistance is reduced to the point where the Joule heating equals the heat flowing to the heat bath. The film thus self-regulates in temperature within its transition, an effect referred to as negative electrothermal feedback.

When an X-ray deposits energy in the absorber, the temperature and resistance of the film increase, leading to a decrease in the current and thus the dissipation of Joule power in the film, while the heat flowing to the heat bath remains approximately constant. Thus, the X-ray energy is primarily removed by a reduction in Joule heating, which can lead to a thermal response time more than a hundred times faster than the natural relaxation time $\tau_0 = C/G$ (Irwin, 1995).

A physical layout and bias circuit of the TES microcalorimeter used in this paper is presented in Fig. 1. The detector has an Ag absorber of area $250 \mu\text{m}$ by $250 \mu\text{m}$ and a thickness of $2 \mu\text{m}$. The absorber is in the centre of a 1 mm by 1 mm TES in order to minimize diffusion times. The TES itself consists of a bilayer of Ag (105 nm thick) and Al (45 nm thick). Ag is a normal metal, and Al is a superconductor with a transition temperature $T_c \approx 1.2$ K. Because of the proximity effect (de Gennes, 1964) the bilayer behaves as a single superconductor with a transition temperature $T_c \approx 120$ mK, causing the detector to self-bias in temperature at 120 mK, well above the regulated temperature (typically 70 mK) of the heat bath. The heat bath is cooled using a compact adiabatic demagnetization refrigerator (ADR), which will be described in a later section. The absorber and thermometer are deposited on a $0.5\text{-}\mu\text{m}$ -thick silicon nitride (Si_3N_4) membrane suspended

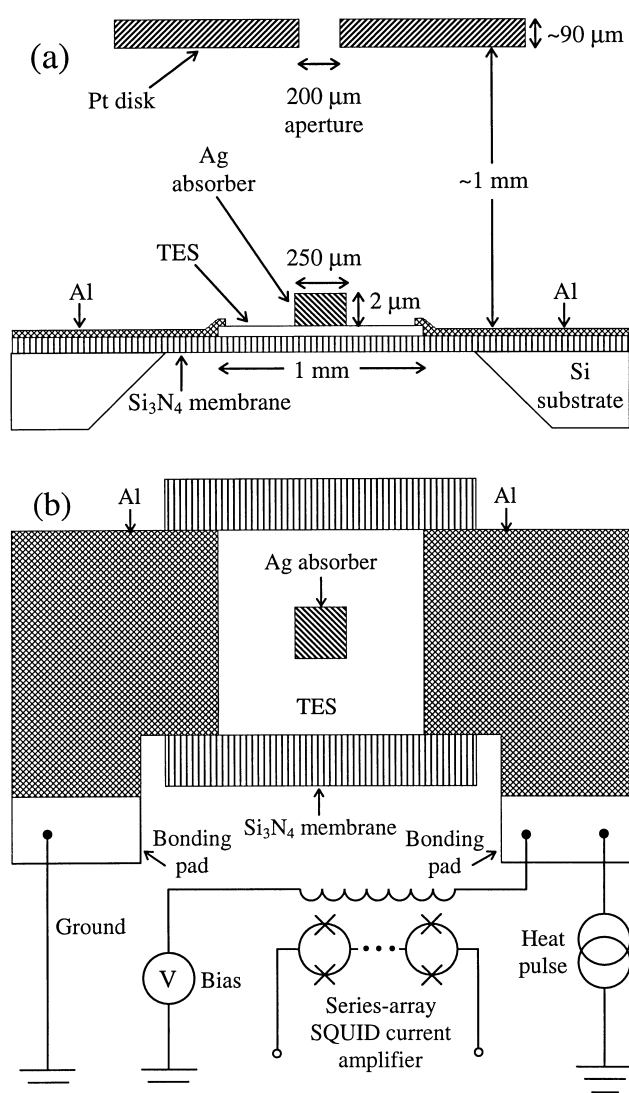


Fig. 1. (a) Cross-sectional drawing of the microcalorimeter detector, not to scale. The TES is a superconducting Al/Ag bilayer (105-nm Ag bottom layer, 45-nm Al top layer), fabricated on a freely suspended 0.5- μm -thick silicon nitride membrane. The normal-metal X-ray absorber, a 2- μm -thick Ag film of area 250 μm by 250 μm , is fabricated on top of the TES. Contacts to the TES are made using 100-nm-thick Al films, which provide both good electrical contact and thermal isolation, since Al has a 1 K superconducting transition that is well above the microcalorimeter operating temperature. Incident X-rays are admitted to the normal-metal absorber through a 200- μm -diameter aperture in a Pt disc. The microcalorimeter was fabricated using thermal evaporation through a series of shadow masks. (b) Top view of the TES microcalorimeter, showing the simplified electrical circuit.

across a hole etched in a silicon substrate. The membrane serves to reduce the thermal coupling between the microcalorimeter and the heat bath, and to help prevent high-energy excitations (from the X-ray) from escaping from the absorber before they are thermalized (Nahum &

Martinis, 1995). Aluminium leads electrically connect the TES to bonding pads. Wire bonds connect the microcalorimeter chip to the electrical bias circuit and SQUID. In addition to the bias leads, an extra lead is attached to the TES to allow the injection of fast pulses of Joule heating which simulate an X-ray event. These heat pulses are used to calibrate the baseline energy resolution without the thermalization and diffusion effects experienced by X-rays. Finally, a 200- μm -diameter aperture in a Pt disc is used to collimate incoming X-rays so that they are incident only on the absorber.

Operation of this detector is complicated by the presence of steps in the current–voltage (IV) characteristics of the film due to the nucleation of phase-slip lines (Skocpol *et al.*, 1974). These features are eliminated by the application of a small magnetic field (≈ 0.2 mT) to the film, driving it into the intermediate state (Tinkham, 1980). A superconducting-aluminium ground plane was deposited on the back side of the silicon nitride membrane. When the detector is cooled through the superconducting transition of aluminium (about 1.2 K), a magnetic field is trapped in the ground plane, and the applied field can be removed. We anticipate that further detector development will eliminate the features due to the nucleation of phase-slip lines and make this field unnecessary.

In later sections we will describe the use of this detector in a complete spectrometer system for real-time X-ray microanalysis in a scanning electron microscope. In the remainder of this section, we will present results obtained with X-rays from a radioactive ^{55}Fe source to characterize the baseline performance of the detector.

The detector was voltage-biased, and pulses of reduced current were observed each time a Mn $K\alpha_{1,2}$ or $K\beta$ X-ray (from the ^{55}Fe source) was absorbed in the microcalorimeter. By biasing the heat bath very near the transition temperature, the intrinsic $1/e$ fall time of the sensor in the absence of electrothermal feedback, $\tau_0 = C/G$, was measured to be about 2.5 ms. When the heat bath was cooled to well below the transition temperature, strong negative electrothermal feedback led to pulses which were more than an order of magnitude faster. Figure 2 shows a typical detector output pulse from the SQUID amplifier in response to a 5.89-keV X-ray. As shown in the inset to Fig. 2, the pulse falls exponentially (linearly when plotted on a logarithmic scale) only for the last part of the pulse. The initial rounding of the pulse is caused by an L/R time constant, where L is the combined stray inductance and inductance of the SQUID input coil and R is the bias resistance of the TES. On the exponential portion of the pulse response, the $1/e$ fall time is about 215 μs . Because of the L/R time constant, the effective pulse duration is somewhat longer. The inductance of the SQUID input coil could be reduced by an order of magnitude for this microcalorimeter without a degradation of the energy resolution.

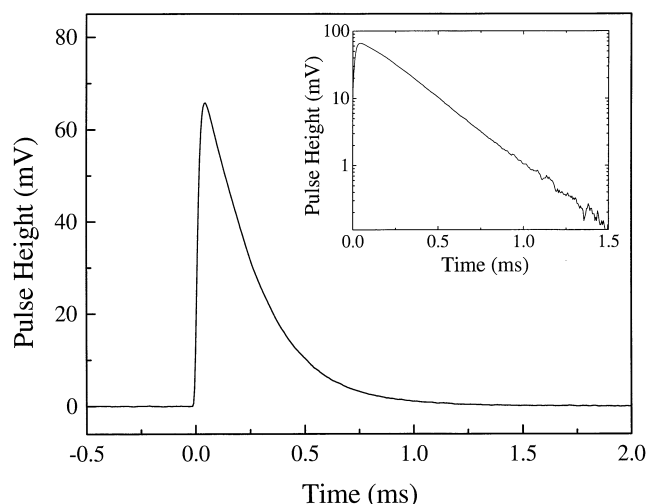


Fig. 2. TES microcalorimeter output pulse from the SQUID amplifier in response to a 5.9-keV Mn $K\alpha$ X-ray. The pulse was shaped by a two-pole low-pass (30 kHz) filter before digitization. As shown in the inset, the pulse is exponential (linear when plotted on a logarithmic scale) for times greater than 0.2 ms, with a corresponding fitted $1/e$ falltime of 215 μ s.

A spectrum of X-ray pulses produced by a radioactive ^{55}Fe source was then collected. The count rate was only about 0.5 counts per second since only a very weak ^{55}Fe source was available, and it was placed several centimetres from the detector outside of the cryostat. A total of 2900 counts was acquired over about 1.5 h. The observed pulses were digitized and analysed using a Wiener optimal filter. When the measured peak heights were plotted as a function of time, we observed a small drift in the temperature of the heat bath (regulated at ≈ 70 mK), which led to a linear drift in the Mn $K\alpha_{1,2}$ X-ray line position of about 3 eV. This linear drift was removed by fitting a line to the peak height vs. time data and subtracting the slope. This drift should be negligible for shorter data sets with faster count rates and should also be improved with better temperature regulation. In addition to X-rays, this data set included 5330-eV pulses of Joule heating which were injected into the TES at regular time intervals.

At the 5.89 keV Mn $K\alpha_{1,2}$ X-ray line, there was an observed differential nonlinearity of 13% in the Wiener filter output. Because the Wiener filter assumes that all pulse shapes are the same, nonlinearity results when energies are high enough to cause variations of pulse shape. In the strong negative electrothermal feedback limit, the pulse energy is removed by a reduction of Joule heating. For a given bias voltage V , a measurement of the integral of the reduced current pulse with the SQUID is thus a direct measure of the pulse energy, $E = \int \Delta P_{\text{joule}} dt = V \int \Delta I d\tau$. If the pulses are integrated instead of optimally filtered, the measured response is very nearly linear at 6 keV. However, the best results were achieved by using the Wiener optimal

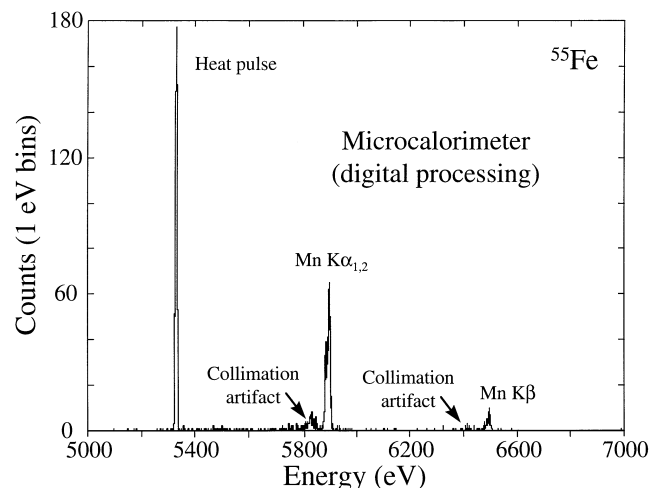


Fig. 3. Microcalorimeter spectrum of ^{55}Fe showing heat pulse (5330 eV), Mn $K\alpha_1$ (5898.75 eV), Mn $K\alpha_2$ (5887.65 eV) and Mn $K\beta$ (6490.45 eV) X-ray lines. The artefacts observed at energies below the Mn $K\alpha_{1,2}$ and Mn $K\beta$ lines result from poor collimation (see text) and are not intrinsic.

filter and then removing the nonlinearity in the data analysis.

In order to remove the nonlinearity, the Wiener-filtered detector response was plotted against the known energies of the heat pulse, Mn $K\alpha_{1,2}$, and Mn $K\beta$ lines. A line was fitted to these three points and used to convert the detector response to a measured energy. Figure 3 is a histogram of the resulting spectrum. In addition to the heat pulse, $K\alpha_{1,2}$ and $K\beta$ lines, an artefact peak is observed at an energy $\approx 10\%$ below each X-ray line. This artefact peak results from X-rays interacting in the TES thermometer instead of the absorber and is due to improper collimation. As will be shown later with spectra taken on the SEM, this peak can be eliminated by improving the collimation.

The measured energy resolution of the 5330-eV heat pulse line was 7.1 ± 0.2 eV FWHM. In order to measure the instrument-response X-ray energy resolution at the Mn $K\alpha_{1,2}$ lines, a convolution of the Gaussian detector response and the Lorentzian natural line widths was fitted to the data using a weighted-least-squares method. The only unconstrained parameters were an amplitude factor determined by the total number of events collected, the Gaussian instrument resolution, and a small offset factor (in energy) to compensate for any residual nonlinearity. In the fit, the variance of the bins with zero data was set to 1.

Following previous work (McCammon *et al.*, 1991; Silver *et al.*, 1996), we used Mn $K\alpha_{1,2}$ energies and linewidths based on a WDS measurement of the Mn $K\alpha_{1,2}$ line shapes (Schnopper, 1967) in the fit, even though the natural line shapes were not deconvolved from the WDS instrument response in Schnopper's measurement. The fit to our

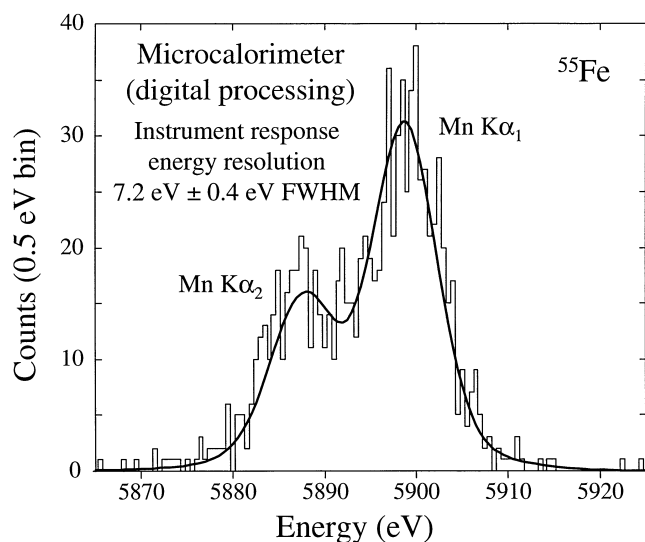


Fig. 4. Weighted least-squares fit of the ^{55}Fe microcalorimeter spectrum to the convolution of the Gaussian instrument response and the Lorentzian natural linewidths of $\text{Mn K}\alpha_1$ (2.13 eV) and $\text{Mn K}\alpha_2$ (2.60 eV). The ratio of the $\text{K}\alpha_2$ peak integral to the $\text{K}\alpha_1$ peak integral is constrained to be 0.5097. The fit yields an instrument-response energy resolution of 7.2 ± 0.4 eV FWHM at 5.89 keV, which is consistent with the heat pulse energy resolution of 7.1 ± 0.2 eV FWHM at 5.33 keV.

microcalorimeter spectrum yielded a Gaussian instrument-response energy resolution of 6.4 ± 0.4 eV FWHM at 5.89 keV. This energy resolution represents a substantial improvement over the best previously reported measurements at 5.89 keV of 7.1 ± 0.7 eV FWHM (Silver *et al.*, 1996) and 7.3 ± 0.4 eV FWHM (McCammon *et al.*, 1991). This result is surprising, however, because then the 6.4 eV energy resolution is better than the 7.1 eV heat-pulse energy resolution. Since the heat pulse line does not have any extra broadening from thermalization and diffusion effects, it is expected to have an energy resolution equal to or better than the X-ray resolution.

In order to resolve this apparent discrepancy, we found in the literature a more recent measurement of the $\text{Mn K}\alpha_{1,2}$ natural linewidths (Lee & Salem, 1974), in which the measured natural line widths were deconvolved from the WDS instrument response. In this work (Lee & Salem, 1974), the Lorentzian natural line widths were determined to be 2.13 eV FWHM for the $\text{K}\alpha_1$ line and 2.60 eV FWHM for the $\text{K}\alpha_{1,2}$ line, both significantly narrower than Schnopper's results. A fit to our data using these reported natural linewidths is shown in Fig. 4 and yields a Gaussian instrument-response energy resolution of 7.2 ± 0.4 eV FWHM. Because this result is in agreement with our heat pulse energy resolution of 7.1 ± 0.2 eV FWHM, and since Lee & Salem deconvolved the natural line width from the detector response, we believe that this result is more reliable. We expect that a reanalysis of the semiconductor-

thermistor microcalorimeter results (McCammon *et al.*, 1991; Silver *et al.*, 1996) using Lee & Salem's $\text{K}\alpha_{1,2}$ natural linewidths will yield energy resolutions of ≈ 8 eV.

Our energy resolution was achieved with a very large heat capacity ($C = 2.5 \text{ pJ K}^{-1}$) and at a detector bias temperature of 120 mK, implying thermodynamic energy fluctuations in the microcalorimeter of $\Delta E_{\text{THERM}} = 2.35\sqrt{(k_B T^2 C)} = 10.4$ eV FWHM. Therefore, for the first time that has been reported, our 7.2-eV detector has an energy resolution that is better than the thermodynamic energy fluctuations in the sensor (by a factor $\xi \approx 0.7$). Further, our value of ξ is about an order of magnitude better than that which has been achieved with silicon-thermistor microcalorimeters ($\xi \approx 7$).

There is still room for improvement in the energy resolution of TES microcalorimeters. The fundamental limit on the energy resolution of a TES microcalorimeter operated in the limit of strong negative electrothermal feedback is about 1.3 eV FWHM at 6 keV for an Au absorber of dimensions $500 \mu\text{m}$ by $500 \mu\text{m}$ by $5 \mu\text{m}$ operated at 100 mK (Irwin, 1995). Better energy resolutions can be achieved for detectors with smaller absorber heat capacities for which nonlinearity occurs at lower energies. We have previously demonstrated heat-pulse energy resolutions of 2.6 eV FWHM at 1 keV and 0.2 eV FWHM at 4 eV for detectors with smaller heat capacities (Irwin *et al.*, 1996).

The response time of our microcalorimeter is currently limited by the critical current of our TES superconducting film. Since the X-ray energy is removed by a reduction in Joule power, and the maximum Joule power dissipation in the film is determined by the critical current, higher critical currents are necessary for faster operation. Our critical current is reduced by more than an order of magnitude by an applied magnetic field to remove the features in the detector IV characteristics due to nucleation of phase-slip lines. We anticipate that further detector development will eliminate the phase-slip line nucleation features without the application of a magnetic field, leading to an improvement in response time of one or two orders of magnitude.

Microcalorimeter spectrometer system

While energy resolutions obtained using digital signal processing with optimal filtering (as described above) suggest the potential usefulness of TES microcalorimeters, a practical microcalorimeter spectrometer system must be developed and fully characterized for X-ray microanalysis under normal real-time operating conditions. Although very important, energy resolution is only one parameter of a complete spectrometer system. Other significant parameters include the geometrical and quantum collection efficiencies, real-time output count rates, energy linearity, ease of use, stability and reproducibility. In this section, we will describe the different components and performance of a complete

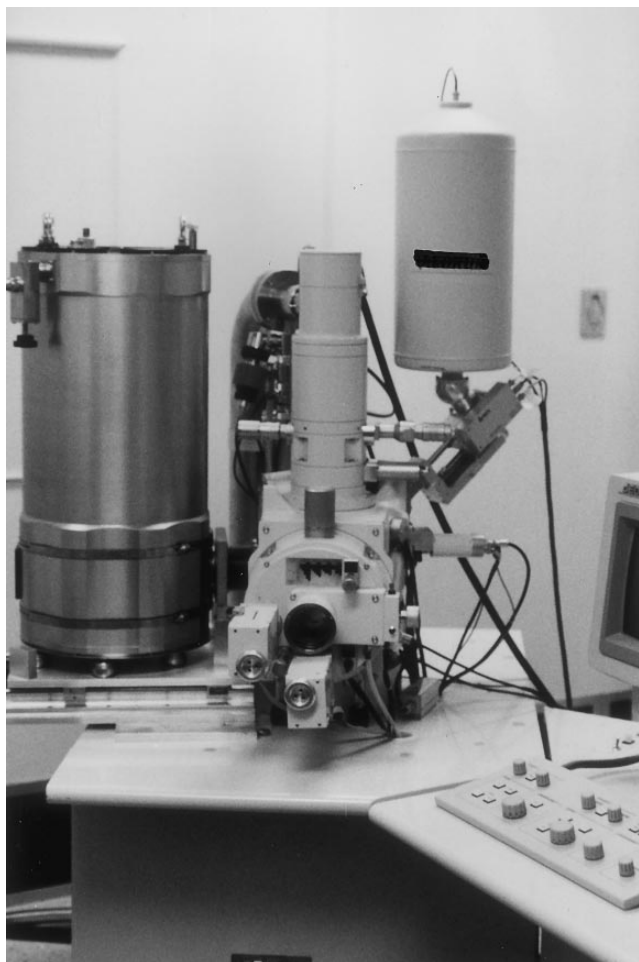


Fig. 5. Photograph of our portable ADR cryostat mounted on the left side of a commercial SEM column. The microcalorimeter is located at the end of a snout (not visible, see Fig. 6) that extends into the SEM. For comparison, a commercial semiconductor EDS system is shown installed on the right side of the column.

microcalorimeter spectrometer system for real-time X-ray microanalysis on an SEM.

Spectrometer refrigeration

Most microscopists are familiar with transferring liquid nitrogen (LN_2) into dewars used to cool Si(Li) and HPGe EDS detectors to ≈ 100 K. X-ray microcalorimeters require substantially lower temperatures of operation, about 100 mK. To reach these low temperatures, we have designed and constructed a compact and portable adiabatic demagnetization refrigerator (ADR) which can be mounted on a commercial SEM, as shown in Fig. 5. A cross-sectional drawing of the ADR is shown in Fig. 6.

In the ADR cryostat (purchased commercially and modified), a series of thermally isolated stages are used to reach the desired 100 mK operating temperature. A LN_2

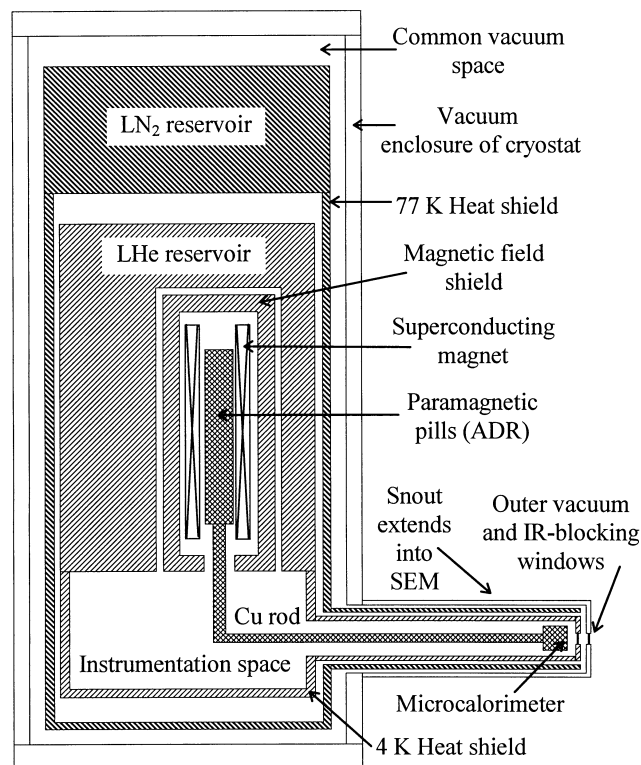


Fig. 6. Cross-sectional drawing of the ADR cryostat, not to scale. The height and diameter of the cylindrical cryostat are 69 and 35 cm, respectively. The length of the snout is 17 cm.

reservoir provides cooling for a 77 K Cu heat shield which surrounds the inner section of the cryostat and intercepts the heat load from room temperature (300 K). A liquid-helium (LHe) reservoir located within the 77 K heat shield provides cooling for a 4 K stage, on which is mounted the series-array SQUID current amplifier, superconducting magnet, magnetic field shield (made of vanadium permendur, an Fe-Co-V alloy), ADR assembly, 4 K Cu heat shield and other electronics. For thermal isolation, the LN_2 , LHe and ADR cold stages are surrounded by a common vacuum space, which is evacuated before cooling and then cryopumped to a very low pressure by the LHe bath. This vacuum space is separated from the vacuum space of the SEM by a commercially available thin-polymer X-ray window.

The ADR is based on a design proposed by Hagmann & Richards (1994). It consists of two paramagnetic pills thermally isolated by tensioned polyparaphenylene terephthalamide (Kevlar) strings, a mechanical heat switch and a superconducting magnet. The paramagnetic pills are composed of a ferric ammonium alum (FAA) salt and a gadolinium-gallium garnet (GGG) crystal. The pills are magnetized in an applied magnetic field of 4 T from a superconducting magnet while connected to the 4 K stage by a mechanical heat switch. After thermal equilibration is

reached, the heat switch is opened and the magnetic field is reduced. Under adiabatic demagnetization (at constant entropy), the temperature of the pills (thermally isolated from 4 K and each other) is reduced as the aligned spins become randomized. Au wires embedded in the FAA pill are used for thermal contact to a long Cu rod, which provides the thermal link between the ADR and the X-ray microcalorimeter. We use a two-pill design (with the GGG pill at 1 K to intercept the heat load from 4 K) to achieve a base temperature of 50 mK from the starting temperature of 4 K by reducing the applied magnetic field to zero. If the magnetic field is not reduced to zero, it is possible to regulate the temperature at a higher value (typically 70 mK) by electronically controlling the current in the superconducting magnet to offset the temperature rise due to small (typically $0.2 \mu\text{W}$) parasitic heat leaks. We have designed and built such a temperature controller for the temperature regulation in the 55 mK to 4 K temperature range. The temperature controller has peak-to-peak temperature fluctuations of less than $20 \mu\text{K}$ for regulated temperatures less than 120 mK.

The overall performance of the ADR is compatible with use in microanalysis applications. The system can operate at a regulated temperature of 70 mK for over 12 h, after which the ADR must be recharged. Recharging the ADR (by ramping up the magnetic field with the heat switch closed, waiting until the ADR is thermally equilibrated at 4 K and ramping down the magnetic field) takes less than 45 min, a process that can be easily scheduled and automated under computer control. The LHe hold time of our ADR cryostat is 4 days (for a 10-L LHe reservoir), with a LN_2 hold time of 2 days. With further cryogenic engineering, it should be possible to increase the liquid helium hold time to approximately 1 week. Because the technology for liquid helium cryogenics is mature, commercial systems will certainly have longer hold times or will even use closed-cycle refrigeration. For direct closed-cycle cooling of the ADR, low-vibration cryocoolers will be necessary to avoid any degradation in electron microscope performance. As an alternative to direct cooling, closed-cycle refrigeration may be used to cool heat shields surrounding the liquid helium reservoir in order to intercept the incident heat and thus significantly extend the liquid helium hold time. This approach benefits from the potential to eliminate vibration by mechanically disconnecting or shutting off the cryocooler during SEM operation.

Our X-ray microcalorimeter is located at the end of the 70 mK Cu cold finger which extends into the SEM and is surrounded by 77 K and 4 K cylindrical Cu heat shields. The spectrometer enters the SEM perpendicular to the electron beam axis, and the sample holder is tilted by 45° toward the spectrometer to allow X-rays to be admitted to the detector, so that the electron-beam entry angle and the X-ray takeoff angle are both 45° . This geometry has been chosen for

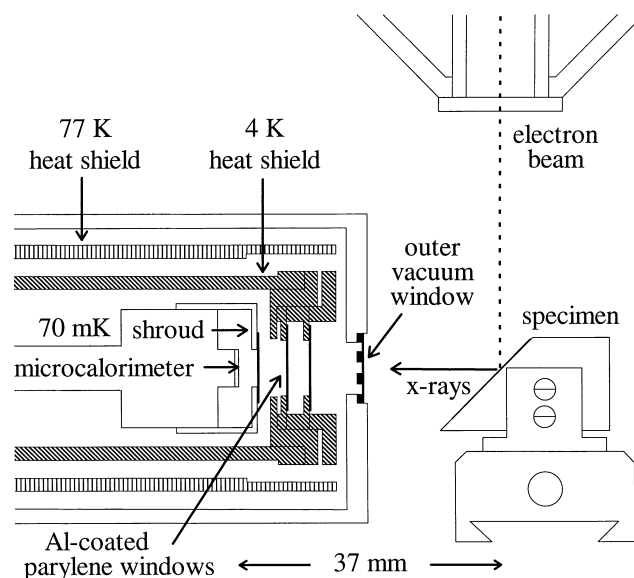


Fig. 7. Cross-sectional drawing of the X-ray windows showing the specimen-detector geometry (approximately to scale). The dimensions of the Si micromachined grid supporting the outer vacuum window have been exaggerated. Freestanding thin Al-coated parylene films at the end of the 4 K heat shield and at the 70 mK shroud are used to attenuate IR radiation. An electron trap located at the end of the snout is not shown.

simplicity and ease of spectrometer development, and can be modified in the future to allow the conventional normal incidence angle between the electron beam and the specimen plane, and a 40° X-ray takeoff angle.

X-rays pass through a series of X-ray windows before arriving at the detector, as shown in Fig. 7. The outer window is a commercially available vacuum-tight thin polymer window supported by a micromachined silicon grid. Two aluminium-coated parylene windows at 4 K and a third at the 70 mK shroud are used to block 300 K infra-red (IR) radiation from reaching the detector. A standard electron trap (a localized magnetic field produced by two permanent magnets, mounted at the end of the snout) is used to prevent high-energy electrons from entering the X-ray microcalorimeter spectrometer. A flexible stainless steel bellows provides the vacuum connection between the ADR and SEM. The mass of the ADR (61 kg) is supported by the main SEM column isolation springs. The ADR sits on a platform that can be mechanically moved in and out of the SEM to adjust the specimen-detector distance, typically 35–40 mm.

Pulse processing

X-ray spectra must be acquired and displayed in real time for practical X-ray microanalysis. For our prototype spectrometer system, this is most easily accomplished with

standard analog filtering and peak height analysis using a conventional EDS multichannel analyser with real-time computer interface. This approach works well because the peak height of the microcalorimeter output pulse is approximately linear in X-ray energy for lower energies, although it is the pulse integral (in the limit of strong electrothermal feedback) that is linear over a much larger energy range, as described previously. However, there are significant benefits to digital processing, as demonstrated by the analysis of the ^{55}Fe spectrum in a previous section. Future microcalorimeter spectrometers will use real-time digital processing for improved performance.

In this section, we describe the analog signal processing and pileup rejection circuitry used to acquire X-ray spectra in real time with our microcalorimeter spectrometer. The analog processing chain begins with a SQUID amplifier output pulse (shown in Fig. 2), which corresponds to the reduction in feedback Joule heating which occurs after an X-ray interacts with the microcalorimeter. A standard linear pulse-shaping spectroscopy amplifier then shapes the SQUID output pulses for peak height analysis using a commercially available EDS multichannel analyser. Because the output pulses are much longer than typical semiconductor EDS detector output pulses, we modified the spectroscopy amplifier to accommodate long-time-duration pulses by increasing the adjustable shaping time constants. These time constants were increased by changing the filter capacitors of the spectroscopy amplifier, along with disabling the pole-zero filter. Output detector pulses from the SQUID amplifier having time constants on the order of $\tau = 250\ \mu\text{s}$ are shaped using a modified pulse-shaping time constant of $34\ \mu\text{s}$ or $51\ \mu\text{s}$ and amplified by an overall gain of ≈ 500 . A DC baseline-restore circuit is used to ensure a stable baseline reference voltage for peak-height analysis.

In parallel with the slow pulse-shaping spectroscopy amplifier, a differentiating circuit and 'fast channel' (shorter time constant) spectroscopy amplifier are used for pulse pileup detection and vetoing of overlapping X-ray pulses. Even though ED spectrometers (both semiconductor and X-ray microcalorimeter) appear to acquire an entire X-ray energy spectrum in parallel, individual X-ray photons absorbed by the detector are processed sequentially. Pulse pileup occurs if there is a second X-ray event at any time during the processing of the preceding X-ray pulse, as determined by an inspection of the fast channel. Because it rides on the tail of the first X-ray pulse, the second X-ray pulse has an (incorrect) increased pulse height and must be rejected for peak height analysis by the multichannel analyser. If the second X-ray pulse arrives before the first has been shaped and reached its peak value, both X-ray pulses must be rejected. If two X-ray photons arrive at the detector in a short time interval and cannot be vetoed by the pulse rejection circuitry, a shaped output pulse corresponding to the sum of the two X-ray photon energies will be

analysed. This leads to 'sum peak' artefacts in X-ray spectra acquired at high count rates.

Proper setting of the discriminator threshold for the detection of fast channel pulses is crucial for correct pileup rejection (Goldstein *et al.*, 1992). Because the fast channel amplifier has a shorter time constant than the slow pulse-shaping amplifier, its output pulses have a higher noise level. A threshold set too low allows noise spikes to cause unnecessary pulse rejection, while a threshold set too high fails to detect low-energy X-ray pulses and leads to degraded energy resolution. Because of the excellent energy resolution of our microcalorimeter, the fast channel has sufficient resolution to discriminate even the lowest energy photons from the noise, resulting in very efficient vetoing. Typical settings include a fast channel amplifier time constant of $7\ \mu\text{s}$, overall gain of 200, and a lower level discriminator threshold of $0.08\text{--}0.13\ \text{V}$, corresponding to an X-ray energy threshold of $\approx 50\text{--}90\ \text{eV}$.

The use of pulse rejection circuitry results in dead time during which pulses cannot be analysed. The dead time τ_{dead} corresponds to the total time duration of an average X-ray pulse extended by an average settling time for the baseline restore circuit. A rough estimate for the dead time is $\tau_{\text{dead}} = 7\tau_{\text{pulse}} = 2\ \text{ms}$, using a typical effective pulse falltime of $\tau_{\text{dead}} = 290\ \mu\text{s}$. The effective falltime (approximately the width of the pulse at $1/e$ of the pulse height) is greater than the typical $1/e$ falltime of $\tau = 215\ \mu\text{s}$ (as obtained from a fit to the exponential portion of the pulse; see Fig. 2) owing to the L/R risetime of the SQUID output signal, as discussed previously. Since X-rays arrive at the detector at times governed by Poisson statistics, the output count rate Γ_{output} is a function of τ_{dead} and the average true input count rate Γ_{input} , such that $\Gamma_{\text{output}} = \Gamma_{\text{input}} \exp(-\Gamma_{\text{input}} \tau_{\text{dead}})$. The maximum count rate that can be achieved is $\Gamma_{\text{max}} = 1/(e\tau_{\text{dead}}) \approx 1/(20\tau_{\text{pulse}})$. With effective microcalorimeter falltimes of $\tau_{\text{pulse}} \approx 250\ \mu\text{s}$ possible for this detector, a maximum count rate of $\Gamma_{\text{max}} \approx 200\ \text{s}^{-1}$ is currently achievable.

With our microcalorimeter spectrometer mounted on an SEM, input and output count rates for X-rays from a Ti foil sample excited by different beam currents were measured experimentally for the X-ray microcalorimeter operated at an effective falltime of $\tau_{\text{pulse}} \approx 310\ \mu\text{s}$. Here, the input count rate is obtained from the fast channel event rate, which provides a good measure of the true input count rate. A fit to these data is shown in Fig. 8, yielding a fitted value of $\tau_{\text{dead}} = 2.25 \pm 0.02\ \text{ms}$, which compares well to the predicted value of $\tau_{\text{dead}} \approx 7\tau_{\text{pulse}} = 2.2\ \text{ms}$.

A related parameter is live time, the time during which X-ray pulses can be analysed. Because an X-ray spectrum is a histogram of analysed pulse energies, the live time of a spectrum is used to compare the normalized X-ray counts of samples and elemental standards for quantitative analysis. The standard procedure is to specify a desired live time,

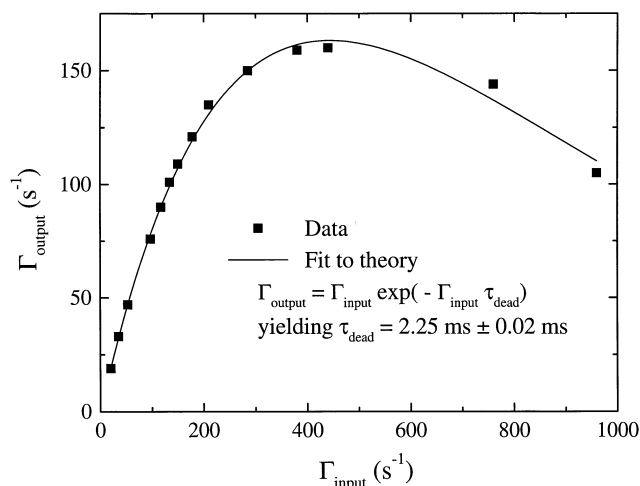


Fig. 8. Output count rate vs. input count rate for a microcalorimeter spectrometer with an effective falltime $\tau_{\text{pulse}} \approx 310 \mu\text{s}$. Also shown is a theoretical fit yielding a fitted dead time of $\tau_{\text{dead}} = 2.25 \pm 0.02 \text{ ms}$.

typically 100 s, and then extend the actual spectrum acquisition time (real time) to compensate for the detector dead time. It is also standard to express the dead time as a percentage,

$$\begin{aligned} DT\% &= \frac{\text{input rate} - \text{output rate}}{\text{input rate}} \cdot 100\% \\ &= \frac{\text{real time} - \text{live time}}{\text{real time}} \cdot 100\%. \end{aligned}$$

Using the analog pulse processing and pileup rejection circuitry described above, shaped microcalorimeter output pulses were analysed using a commercially available multichannel analyser that could directly acquire X-ray spectra into Desktop Spectrum Analyser (DTSA), an NIST X-ray spectrum analyser program developed by Fiori *et al.* (1991). Figure 9 shows a real-time spectrum of AlGaAs obtained with our microcalorimeter spectrometer mounted on a commercial SEM, acquired directly into DTSA. The raw spectrum data consist of X-ray counts vs. channel number for 4096 total channels with a nominal binwidth of 1 eV per channel.

In order to convert from channels to energy in this spectrum, it is necessary to determine the linearity of the detector response as a function of energy. In a semiconductor EDS detector, shaped output pulse heights are very nearly linear as a function of energy over the entire energy range. As described previously, for a TES microcalorimeter operating in the limit of strong electrothermal feedback, it is the pulse integral that is very nearly linear with X-ray energy, even for X-ray energies large enough (compared with the heat capacity of the microcalorimeter) to saturate the TES thermometer. While it may be possible to exploit this pulse integration in the future using real-time digital

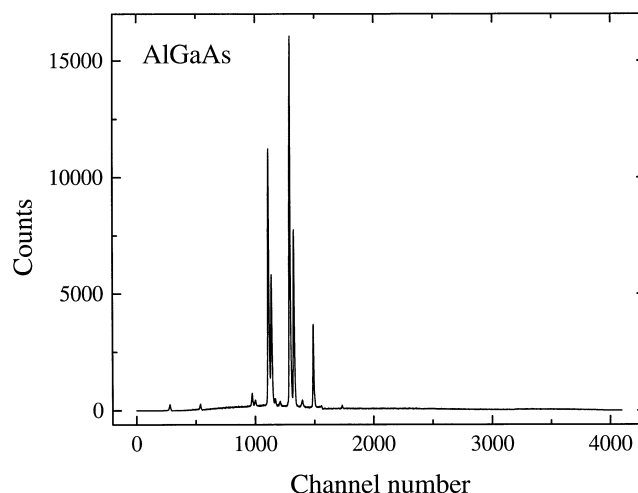


Fig. 9. Microcalorimeter spectrum of AlGaAs. This spectrum was taken under the following conditions: 5 keV beam voltage, 56 nA beam current, input count rate of $145 \pm 10 \text{ s}^{-1}$, output count rate of $115 \pm 5 \text{ s}^{-1}$, dead time of $20 \pm 3\%$, live time 6000 s, specimen-detector distance of $37 \pm 2 \text{ mm}$, and a total of 837 636 counts.

pulse processing, for the analog pulse processing described here, the microcalorimeter is operated at X-ray energies at which there is only a small ($\approx 10\%$) differential nonlinearity in the plot of output peak height as a function of input energy. To correct for this nonlinearity in acquired microcalorimeter spectra, we determine experimentally the channel-to-energy conversion by fitting measured peak channels to known X-ray peak energies over the entire energy range of interest, as shown in Fig. 10(a) for the AlGaAs data set. The least-squares fit of a fifth-order polynomial to data corresponds to a third-order gain correction to the linear gain and offset of the multichannel analyser. The figure also shows a fit to the energy nonlinearity of a more complete, multiple element data set with many characteristic X-ray lines covering a larger energy range. As shown in Fig. 10(b), the residuals of both fits are on the order of 2 eV, consistent with the uncertainty in the experimental determination of the peak channel positions. In the future, it may be possible to linearize the measured peak height nonlinearity (before pulses are analysed with a multichannel analyser) with the use of a computer-programmable nonlinear gain circuit, which we have designed and are currently testing.

Using the fitted channel-to-energy conversion described above, the resulting AlGaAs spectrum of X-ray counts vs. energy is shown in Fig. 11 for the energy range 900–1700 eV. The energy binwidth per channel varies from 1.01 to 1.02 eV over this range. For energy regions of the spectrum in which the energy binwidth per channel varies significantly, one can normalize the X-ray counts per channel by dividing by the respective energy binwidth.

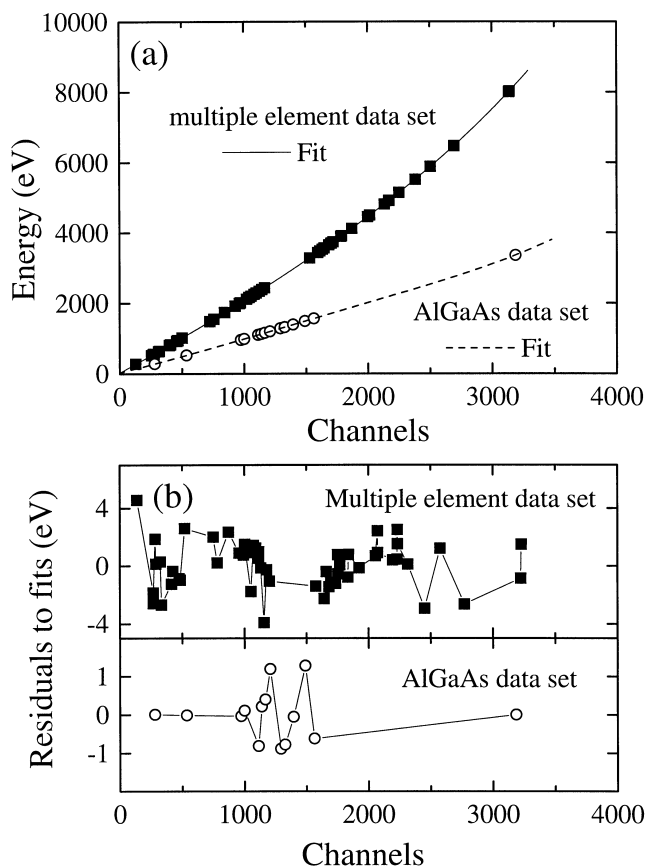


Fig. 10. (a) Fifth-order polynomial least-squares fits to the peak channel position vs. known X-ray line energy for the AlGaAs data set (open circles) and a multiple element data set (filled circles). The data points are larger than the size of the error bars associated with the fitted peak channel positions. Note that the multiple element data set covers a larger energy range (vertical axis) than the AlGaAs data set. (b) Residuals of the fits to the AlGaAs and multiple element data sets.

Another option is to rebin the experimental spectrum using binwidths of equal energy (assuming that all X-ray counts are evenly spaced in a given channel), which at the present time is required if the spectrum modelling and analysis features of DTSA are to be used. Rebinning should be avoided whenever possible, however, to avoid the potential loss of statistical information and the introduction of peak shape distortions.

A normalized AlGaAs spectrum is shown in Fig. 12 using a logarithmic scale plot to emphasize the X-ray bremsstrahlung background. In addition to the Al-K, Ga-L and As-L peaks, X-ray peaks corresponding to Si, O and C contaminants are visible. The measured X-ray bremsstrahlung background clearly shows the presence of strong absorption edges corresponding to C (284 eV), O (532 eV), Al (1559 eV) and Ag (3351 eV). These absorption edges are directly related to the overall spectrometer efficiency, which

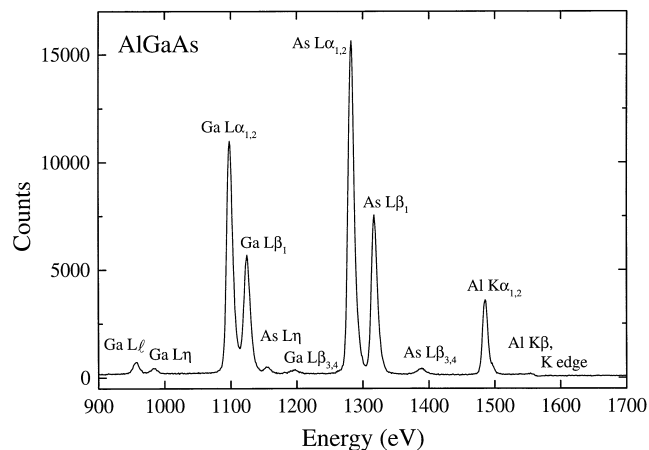


Fig. 11. Microcalorimeter spectrum of AlGaAs from 900 to 1700 eV, corrected for energy nonlinearity. The energy binwidth per channel varies from 1.01 to 1.02 eV over this energy range.

is the product of the X-ray window transmission and the X-ray absorption efficiency of the Ag absorber of the microcalorimeter.

Spectrometer efficiency

The overall spectrometer efficiency can be modelled as a function of energy using tabulated mass absorption coefficients and known window elemental compositions. The calculated spectrometer efficiency is useful for local background subtraction and quantitative comparisons between generated and experimentally measured X-ray spectra. Low-Z (atomic number), low-density X-ray windows are used to improve the transmission of low-energy X-rays. A cross-sectional diagram indicating the location of the different X-ray windows and the specimen–detector distance was shown in Fig. 7.

The outer window is a commercially available vacuum-tight polymer window. The window consists of a 300-nm-thick membrane composed of alternating layers of polymer and aluminium, and is supported by a micromachined Si grid. The polymer has an elemental composition of H, C, N and O, all low-Z elements. The calculated X-ray transmission vs. energy for this polymer window (without the Si supporting grid) is plotted as a solid line in Fig. 13.

The support structure consists of long, parallel micro-machined Si bars that are typically 50 μm wide, 380 μm thick and are separated by 200 μm . X-ray transmission is spatially modulated, as incident X-rays are stopped by the thick Si bars, but pass through the open areas. For a large area detector, the X-ray transmission efficiency of the Si support grid is averaged over many periods of modulation, and is thus determined by its open area, typically 75–80%. Owing to the thickness of the Si bars, the X-ray transmission is largely independent of energy. For the

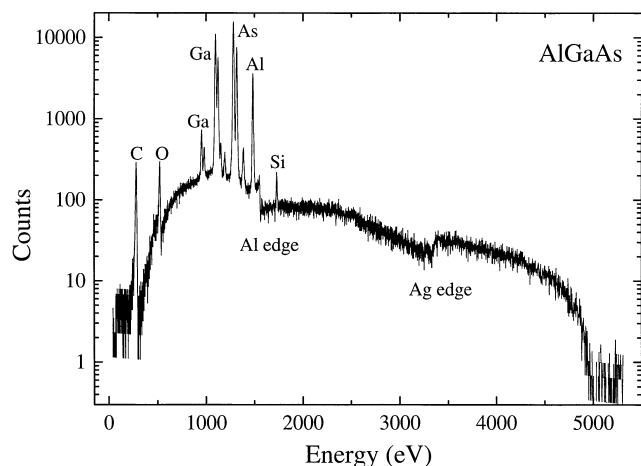


Fig. 12. Normalized microcalorimeter spectrum of AlGaAs, corrected for energy nonlinearity. The X-ray counts per channel have been normalized by the energy binwidth of each channel, which slowly increases from 0.9 eV at 200 eV to 1.1 eV at 2700 eV, then rises to 3 eV at 5 keV.

microcalorimeter, however, the area of the shadowed region of the Si grid is significant compared with the small area (250 μm by 250 μm) of the normal-metal (Ag or Au) absorber. As the electron beam in the SEM (and thus the position of the X-ray source) is scanned over large areas, the region of the normal-metal absorber that is shadowed by the Si grid varies in location and size. Depending on the relative orientation of the grid and the absorber as well as the sample-to-detector and sample-to-grid distances, the area of the shadowed region can vary from 0% to over 50% of the total absorber area. The standard experimental procedure is to scan the electron beam to maximize the input count rate of the spectrometer, resulting in a typical Si grid X-ray transmission efficiency on the order of 90% for a specimen-detector distance of 37 mm.

In addition to the outer vacuum window, additional filters are required to greatly attenuate the room-temperature IR radiation incident on the cryogenic detector. This attenuation is necessary to minimize the overall heat load and (more significantly) to avoid additional detector noise caused by IR photon shot noise. To satisfy the latter requirement, it is necessary to attenuate the IR radiation by roughly 10 orders of magnitude (McCammon *et al.*, 1991). Taking advantage of the large real part of the refractive index of aluminium in the IR, several thin Al-coated parylene windows (two at 4 K, and one at 70 mK) are used to attenuate the IR radiation by reflection. Each filter consists of ≈ 140 nm of Al evaporated on a free-standing parylene film (100 nm thick) which is supported by a mounting ring. A close-packed set of windows is used to minimize the distance between the specimen and the detector. In this geometry it is difficult to reduce multiple IR reflections, making it necessary to use thicker than

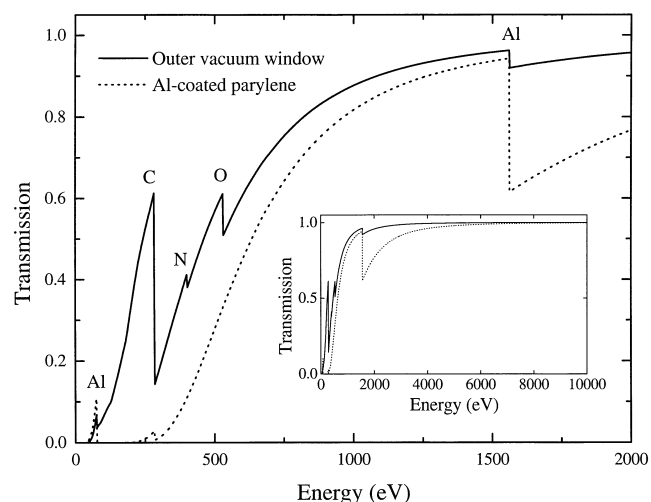


Fig. 13. Calculated X-ray transmission of the outer vacuum window (solid line) and the three Al-coated parylene windows (dashed line).

optimum Al layers to achieve the desired attenuation. The calculated X-ray transmission of the three Al-coated parylene windows is shown in Fig. 13, as indicated by the dashed line. In order to improve the overall low-energy X-ray window transmission, work is in progress to minimize the necessary Al thickness by using IR-absorbing ('black') coatings between filters.

The probability of X-ray absorption in the microcalorimeter absorber also contributes to the overall microcalorimeter spectrometer efficiency. The choice of absorber material is determined by several factors. As described previously, the use of a very sensitive TES thermometer in our microcalorimeter allows us to use normal-metal absorbers with higher heat capacity and better X-ray thermalization properties than the semiconducting or superconducting absorbers which must be used with semiconductor-thermistor microcalorimeters. For the effective capture of incident X-ray photons, high-Z absorbers are desirable for their high densities and large overall mass absorption coefficients. Additionally, absorber materials should be convenient for ease of device fabrication, and should be stable over long periods of time. Two elements that satisfy these requirements are Ag and Au, both of which are metals with relatively low heat capacity at 100 mK. Although Au absorbers are preferred for their higher Z and density (and will be used in future TES microcalorimeters), an Ag absorber was used in the TES microcalorimeter reported here for reasons of process simplicity and cost.

The X-ray photoelectric absorption efficiency of this 2-m-thick Ag absorber is calculated using tabulated mass absorption coefficients and is plotted as a function of energy in Fig. 14. Ag absorption edges are found at 3351, 3523.6 and 3805.6 eV. For comparison, the efficiency of a

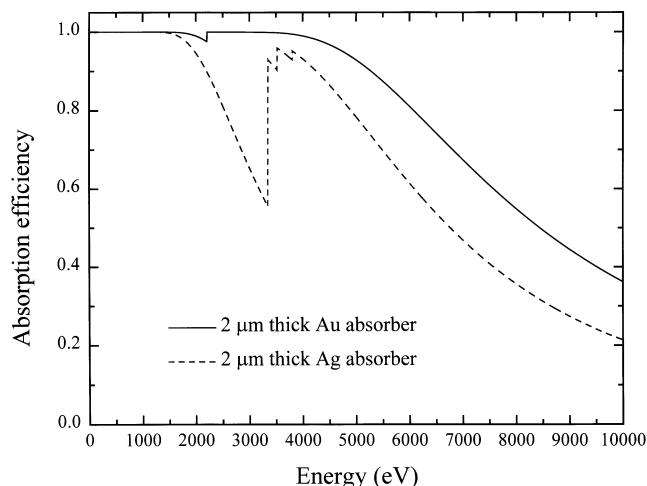


Fig. 14. Calculated absorption efficiency of a 2- μm -thick Au absorber (solid line) and a 2- μm -thick Ag absorber (dashed line).

2- μm -thick Au absorber is also plotted, showing a small absorption edge at 2205.6 eV. Further development of our microcalorimeter should allow the use of an Au absorber up to 5 μm thick, with an efficiency greater than 99% at 6 keV. It is also possible to further increase the efficiency at higher energies by capping the Au absorber with Bi, a high-Z, low-heat-capacity semimetal.

The overall spectrometer efficiency for the microcalorimeter reported here is obtained by multiplying the total X-ray window transmission by the absorber efficiency and is shown in Fig. 15. The X-ray transmission of the outer and IR-blocking windows and the Si grid transmission, and the Ag absorber efficiency are also shown for comparison. The overall spectrometer efficiency can be improved by using a

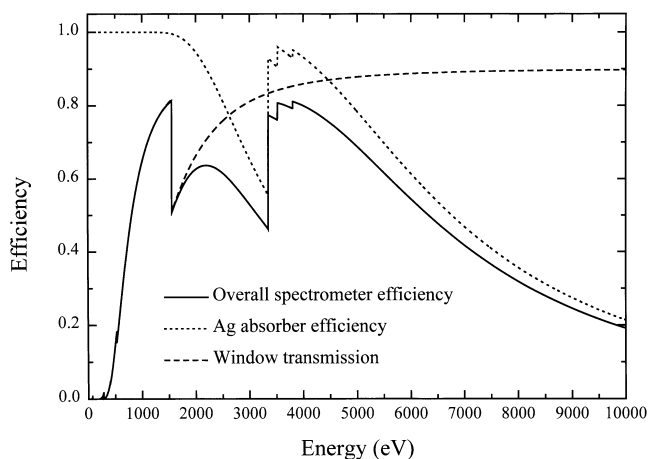


Fig. 15. Overall microcalorimeter spectrometer efficiency (solid line) as a function of energy. Also shown are the absorber efficiency of the 2- μm -thick Ag absorber (dotted line) and the combined X-ray window transmission (dashed line) of the outer and IR-blocking windows (460 nm Al, 300 nm parylene, and 300 nm vacuum-window polymer) and Si grid transmission (90%).

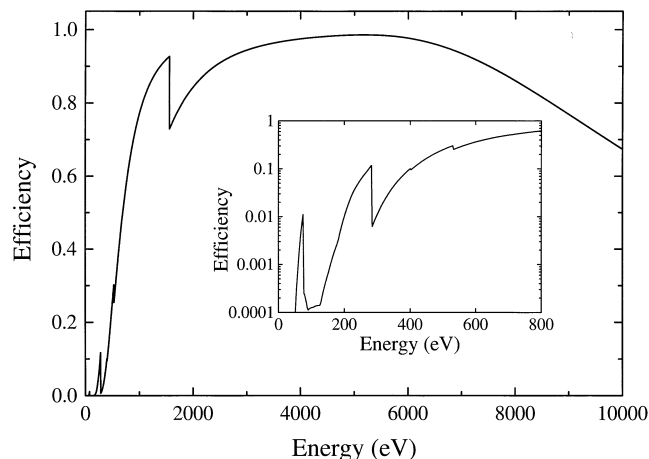


Fig. 16. Overall microcalorimeter spectrometer efficiency that may be achieved in the future, assuming a 5- μm -thick rectangular Au absorber and 65-nm-thick Al for each IR-blocking filter.

thicker (5 μm) rectangular Au absorber and by reducing the Al thickness of each IR-blocking filter to less than 70 nm, with the resulting spectrometer efficiency shown in Fig. 16.

An X-ray spectrum of a spectroscopically pure carbon disc was acquired to check the calculated spectrometer efficiency. The spectrum was corrected for energy non-linearity and rebinned using a uniform binwidth of 2 eV, and is shown in Fig. 17. Owing to a misalignment of the spectrometer axis with respect to position of the electron beam on the carbon disc, X-rays from the sample passed through the Si grid of the outer vacuum window at a relatively large incidence angle ($\approx 4^\circ$ from the axis perpendicular to the plane of the Si grid), such that the typical Si grid transmission was reduced from $\approx 60\%$ to $\approx 20\%$. A carbon bremsstrahlung X-ray spectrum was generated from the known experimental parameters and assumed spectrometer efficiency using DTSA and is also shown in Fig. 17. Although there is qualitative agreement between the generated and experimental spectra, the calculated spectrometer efficiency overestimates the actual spectrometer efficiency at low energies. This difference is not surprising, as it is difficult to accurately calculate the X-ray transmission of the thin polymer vacuum window, particularly at a nonzero incidence angle. In addition to the predicted C peak and C, O, Al and Ag edges observed in the bremsstrahlung background of the microcalorimeter spectrum, an O K α peak (at 522 eV) is observed. This peak can be explained by the presence of oxygen in hydrocarbon contaminants on the surface of the carbon disc, particularly since a contamination spot at the fixed electron beam position was clearly visible after the spectrum was acquired.

Spectral artefacts

In addition to overall spectrometer efficiency, other artefacts

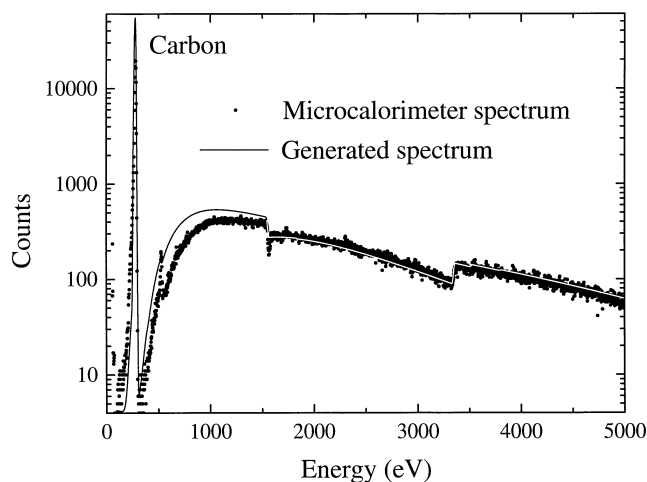


Fig. 17. Microcalorimeter X-ray spectrum (solid circles) of a spectroscopically pure C disc, plotted on a logarithmic scale to emphasize the bremsstrahlung background. The microcalorimeter spectrum was obtained under the following conditions: 10 keV beam voltage, 254 nA beam current, input count rate of $200 \pm 10 \text{ s}^{-1}$, output count rate of $150 \pm 5 \text{ s}^{-1}$, dead time of $25 \pm 4\%$, live time 3074 s, sample-to-detector distance of $37 \pm 2 \text{ mm}$, and a total of 608 646 counts. The spectrum was corrected for energy nonlinearity and rebinned with a uniform binwidth of 2 eV. The rebinning method used here assumes that all X-ray counts are evenly spaced in each channel. Also shown is a C bremsstrahlung spectrum (solid line, plotted in white above 1550 eV) generated from the known experimental parameters and assumed spectrometer efficiency using DTSA. The generated and microcalorimeter spectra are in agreement above 5 keV (not shown) and fall smoothly to zero.

of detection can affect the measured X-ray spectra. It is important to understand the source of potential artefacts, both correctable and intrinsic, and account for their presence in experimental spectra to avoid incorrect identification and quantification of X-ray peaks. Overall, our microcalorimeter spectrometer is free from gross artefacts, as demonstrated by the clean carbon bremsstrahlung spectrum shown in Fig. 17.

As an example of a correctable spectrum artefact, a small parasitic peak on the low-energy side of a parent X-ray peak was observed in initial spectra obtained with an ^{55}Fe source, as described previously. With the microcalorimeter spectrometer mounted on an SEM, this artefact varied in magnitude (but not energy) with the beam position on the specimen, ranging from a well-separated, sharp minor peak to a negligible or nonexistent peak. This behaviour is shown for two Al spectra superimposed in Fig. 18 and suggests a collimation effect, since different regions of the microcalorimeter are shadowed by the Si grid of the outer vacuum window as the beam position is changed. In particular, X-rays that are absorbed directly in the TES produce a slightly lower output peak height than X-rays of the same energy that interact with the normal-metal

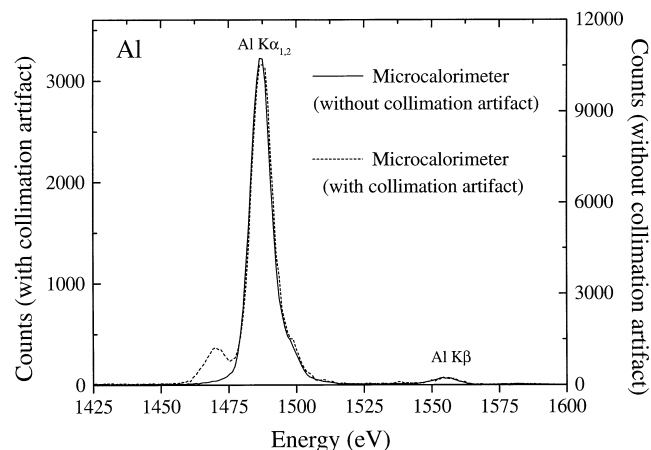


Fig. 18. Two microcalorimeter spectra of Al at different electron beam positions on the specimen, separated by 2 mm. The spectrum with the low-energy satellite was acquired under the following conditions: 5 keV beam voltage, 63 nA beam current, input count rate of $185 \pm 20 \text{ s}^{-1}$, output count rate of $135 \pm 10 \text{ s}^{-1}$, dead time of $27 \pm 5\%$, live time 300 s, sample-to-detector distance of $37 \pm 2 \text{ mm}$, and a total of 53 838 counts. The spectrum without the low-energy satellite was acquired under the following conditions: 5 keV beam voltage, 63.8 nA beam current, input count rate of $160 \pm 10 \text{ s}^{-1}$, output count rate of $120 \pm 5 \text{ s}^{-1}$, dead time of $25 \pm 5\%$, live time 1000 s, specimen-detector distance of $37 \pm 2 \text{ mm}$, and a total of 154 522 counts. Both spectra were identically corrected for energy nonlinearity. The energy binwidth per channel is 1.024 eV. The left and right vertical axes refer to the spectra with and without the collimation artefact, respectively.

absorber. This effect leads to the formation of the observed lower energy parasitic peak, which can be eliminated by using a correctly aligned mechanical collimator that is centred over the absorber and prevents X-rays from interacting directly with the TES. Other correctable artefacts, such as sum peaks, arise from inadequate pulse pileup rejection and have been discussed previously.

Intrinsic artefacts are particularly important to understand because they cannot be eliminated. Both microcalorimeter and semiconductor ED spectrometers are susceptible to intrinsic artefacts owing to the nature of the measurement process, in which X-rays interact directly with the detector to produce a signal proportional to energy. The initial photoelectric absorption of an X-ray in the detector results in the ejection of a core-level electron and the subsequent emission of an Auger electron or characteristic X-ray photon as the ionized atom relaxes to its ground state energy. The original photoelectron and Auger electron typically have short ranges (several hundred nanometres) before they are down-converted in energy and reabsorbed in the detector. The characteristic photon, however, has a substantially longer range. In an Si(Li) detector, the range of Si $K\alpha$ X-rays (in Si) is $36.5 \mu\text{m}$ for 95% attenuation, compared with ranges of $5.6 \mu\text{m}$ in the normal-metal

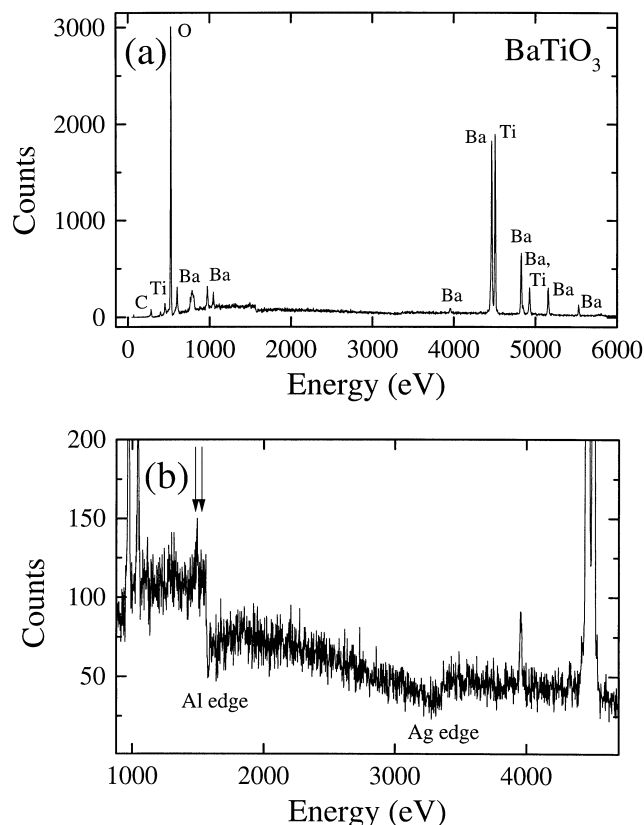


Fig. 19. (a) Microcalorimeter spectrum of BaTiO_3 acquired under the following conditions: 10 keV beam voltage, 68 nA beam current, input count rate of $135 \pm 5 \text{ s}^{-1}$, output count rate of $100 \pm 5 \text{ s}^{-1}$, dead time of $26 \pm 3\%$, live time 1500 s, specimen–detector distance of $37 \pm 2 \text{ mm}$, and a total of 198 692 counts. The spectrum was corrected for energy nonlinearity. The energy binwidth per channel increases from 2.0 eV at 600 eV to 3.2 eV at 6000 eV. (b) Same spectrum presented with expanded horizontal and vertical scales to look for the presence of Ag escape peaks at 1482 and 1527 eV, as indicated by the two arrows. The small observed peak (between the two arrows) may also arise from Al fluorescence in the IR-blocking filters.

absorber of the microcalorimeter for Ag $L\alpha$ X-rays (in Ag) and $1.5 \mu\text{m}$ for Au $M\alpha$ X-rays (in Au). If the characteristic photon escapes from the detector, its energy is lost and will not be included in the total energy measured, resulting in an escape peak in acquired X-ray spectra at an energy lower than that of the parent. The difference in energy between the parent and escape peaks is equal to the energy of the escaped photon.

Escape peaks are a familiar phenomenon in semiconductor EDS systems, where the magnitude of the escape peak can be as great as 2% of the parent. Escape peaks are also expected for the microcalorimeter reported here, since the range of Ag $L\alpha$ X-rays in Ag ($5.6 \mu\text{m}$) is greater than the $2 \mu\text{m}$ absorber thickness. A spectrum of BaTiO_3 , shown in Fig. 19, was examined for the presence of predicted escape

peaks at energies of 1482 eV and 1527 eV, obtained by subtracting the Ag $L\alpha_1$ energy (2984 eV) from the Ba $L\alpha_1$ (4466 eV) and Ti $K\alpha_1$ (4511 eV) energies. Unfortunately, these energies are close to the energy of the Al $K\alpha$ line (1487 eV) and the Al $K\alpha$ edge (1560 eV). A small Al $K\alpha$ contribution is expected to be present as a result of fluorescence in the IR-blocking filters. One small peak can be observed at an energy of 1492 eV and contains roughly 130 counts above background, which represents $\approx 0.5\%$ of the integrated counts of the Ba $L\alpha$ and Ti $K\alpha$ lines. The absence of a large escape peak can be explained by the low effective fluorescence yield for Ag $L\alpha$ X-rays, reported to be 6% (Krause, 1979). The low fluorescence yield indicates that most initial ionizations result in Auger electron emission instead of characteristic X-ray photon generation.

A more subtle intrinsic artefact related to escape peaks is the appearance of a background shelf, in which the measured continuum background is increased slightly at all energies below a parent X-ray peak. This very broad artefact results from additional sources of incomplete energy collection, such as the escape of continuum X-rays generated by inelastic scattering of the initial energetic photoelectron. In semiconductor ED spectrometers, the total integrated background shelf represents $\approx 1\%$ of the counts in the integrated parent peak (Goldstein *et al.*, 1992), and is most easily observed in spectra acquired using a radioactive ^{55}Fe source that emits only Mn-K X-rays. Initial digitally processed microcalorimeter spectra acquired using a weak ^{55}Fe source (as described in a previous section) did not have statistically significant X-ray counts to confirm or quantify the presence of escape peaks and a background shelf. In the future, a stronger ^{55}Fe source will be used to fully characterize microcalorimeter performance.

Energy resolution

We now consider the energy resolution that can be achieved for real-time spectrum acquisition using our microcalorimeter spectrometer mounted on an SEM. Degradation in energy resolution is caused by independent components of the pulse processing chain, which are added in quadrature to the baseline microcalorimeter energy resolution of $7.2 \pm 0.4 \text{ eV}$ for 5.89 keV Mn $K\alpha_{1,2}$ X-rays from an ^{55}Fe source. The measured baseline detector energy resolution includes the intrinsic energy resolution of the microcalorimeter operated with electrothermal feedback and the resolution broadening associated with noise introduced by the SQUID electronics.

A significant degradation in energy resolution is caused by the nonoptimal analog shaping of the output pulse. The deterioration of the signal-to-noise ratio due to the four-pole active filter network of the pulse-shaping linear amplifier is $\approx 17\%$, resulting in a energy resolution at 6 keV that is degraded from 7.2 eV FWHM to 8.4 eV FWHM. Because the

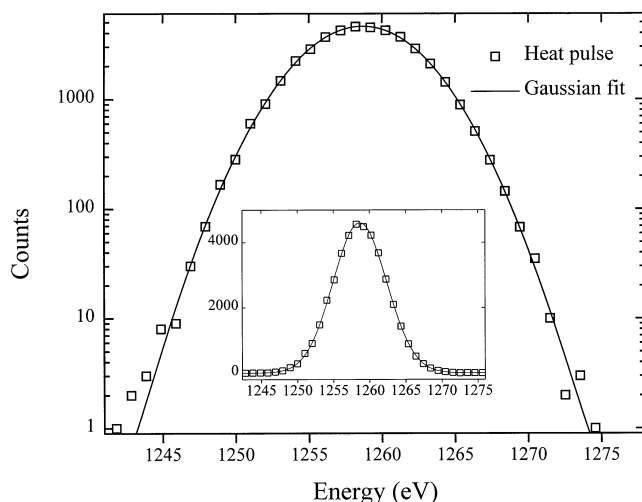


Fig. 20. Microcalorimeter spectrum of a monoenergetic heat pulse (open squares, plotted on a logarithmic scale), acquired as part of the AlGaAs data set and corrected for energy nonlinearity. Also shown is a Gaussian fit (solid line) to the data with a fitted peak centre of 1258.7 eV and a fitted energy resolution of 8.73 ± 0.03 eV (FWHM). Note that good agreement between the Gaussian fit and the data is observed, even at the tails. The indicated uncertainty (0.03 eV) represents the statistical uncertainty in the energy resolution, which was fitted using the standard Levenberg–Marquardt algorithm, with square roots of the data points used as weights. Including an estimate of the uncertainty introduced by the energy nonlinearity correction results in a heat-pulse instrument-response energy resolution of 8.7 ± 0.1 eV (FWHM). A plot of the same data on a linear scale is shown in the inset.

amplifier was modified to provide longer pulse-shaping time constants, resulting in a decreased noise bandwidth, the additional noise contribution of the linear amplifier to the 8.4 eV energy resolution was reduced to less than 1 eV FWHM and thus can be neglected.

Another potential source of energy resolution degradation is the multichannel analyser used to analyse the shaped output peak heights. The performance of the multichannel analyser was measured experimentally using generated low-noise pulses, and it was found that the multichannel analyser contributes an energy resolution degradation of ≈ 1.5 channels FWHM in the SEM noise environment. This degradation is negligible if measured X-ray peaks are spanned by a sufficiently large number of channels. This requirement is difficult to satisfy, however, because of the high energy resolution of the microcalorimeter and the limit of 4096 channels for most commercially available multichannel analysers for EDS spectrometry. The experimental spectra reported here typically cover energy ranges up to 5 keV or 10 keV using a multichannel analyser with 4096 channels. Typical energy binwidths are on the order of 1–3 eV per channel and increase with channel number owing to the nonlinearity of the microcalorimeter

at high energies. These binwidths imply an energy resolution broadening on the order of ≈ 1.5 eV FWHM for 5 keV spectra and ≈ 3 eV FWHM for 10 keV spectra, with the energy resolution degradation increasing at higher energies. This degradation will be reduced significantly in the future with the use of multichannel analysers for EDS spectrometry with over 16 000 channels.

Temperature regulation is another source of degraded energy resolution. Because the TES is a very sensitive thermometer (within its narrow superconducting transition), the microcalorimeter operated without electrothermal feedback (ETF) would be very sensitive to fluctuations in the regulated temperature of the ADR. When operated with ETF, the TES self-regulates in temperature, and the microcalorimeter is much less sensitive to fluctuations in the temperature of the heat bath. As a measure of this sensitivity, a linear drift in the output pulse heights of 3 eV was observed over 1.5 h in the digitally processed ^{55}Fe spectrum described in a previous section. In this case, the detector self-regulated at 120 mK, and the output pulse height drift corresponded to a change of ≈ 30 μK in the regulated temperature of the heat bath (70 mK). This temperature drift is consistent with the observed temperature fluctuations of the RuO_2 thermometer used for temperature regulation (≈ 20 μK short-term peak-to-peak fluctuations, ≈ 20 μK to ≈ 30 μK longer term temperature excursions). Therefore, we estimate that fluctuations in the temperature of the regulated heat bath contribute an energy resolution degradation of ≈ 3 eV, which can be reduced significantly with improved temperature regulation.

The different contributions to the energy resolution degradation for analog processing and real-time spectrum acquisition are then added in quadrature to obtain an estimate for the overall instrument-response energy resolution of ≈ 10 eV at 6 keV, assuming an energy binwidth of 3 eV per channel. This value is larger than the 7.2 ± 0.4 eV FWHM obtained for optimally filtered digitized pulses from an ^{55}Fe source, but can in principle be improved to ≈ 8.6 eV for this detector through better temperature regulation and more channels in our peak height analyser channels. The actual energy resolution of the microcalorimeter spectrometer mounted on the SEM is typically larger than 10 eV at 6 keV owing to nonoptimal detector biasing and additional noise sources such as ground loops and field noise.

Experimental determination of energy resolution

In order to independently measure the energy resolution that can be achieved for X-rays using our microcalorimeter spectrometer, we simulate X-ray events using fast heat pulses dissipated in the normal-metal absorber, as described in a previous section. Unlike electronic pulsers used to measure electronic noise in semiconductor EDS systems,

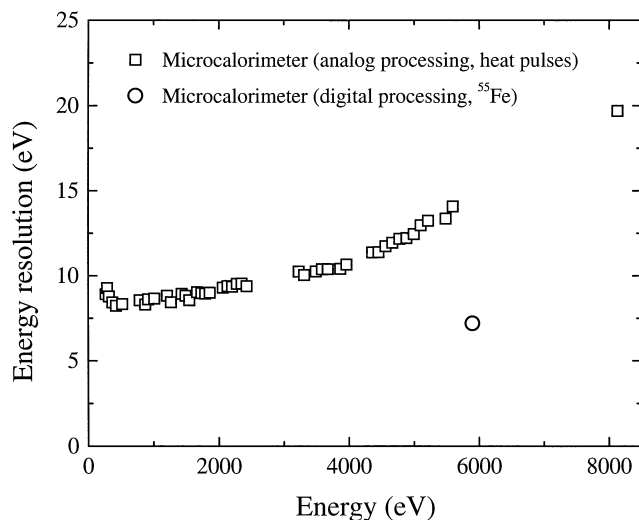


Fig. 21. Typical microcalorimeter instrument-response energy resolution (FWHM) as a function of energy (open squares), as determined from heat pulse spectra. The statistical uncertainty in the data from the Gaussian fitting procedure is smaller than the size of the data points. The overall uncertainty in the data (0.3 eV), including the uncertainty due to the energy nonlinearity correction, is indicated by the size of the data points. Also shown (open circle) is the best instrument-response energy resolution of $7.2 \pm 0.4\text{ eV}$ FWHM at 5.89 keV for this microcalorimeter, obtained from a careful analysis of optimally filtered digitized pulses obtained using a radioactive ^{55}Fe source (see text).

heat pulses allow the combined response of the microcalorimeter and the pulse-processing electronics to be characterized. A spectrum of monoenergetic heat pulses can therefore be used to obtain the energy resolution of our microcalorimeter spectrometer, independent from acquired X-ray spectra.

An example of a monoenergetic heat pulse spectrum is shown in Fig. 20. This spectrum was acquired at the same time as the AlGaAs data set presented previously and has been corrected for energy nonlinearity. The heat pulse peak is very well fitted, even in its tails, by a Gaussian curve with an energy resolution of $8.7 \pm 0.1\text{ eV}$ FWHM at 1258.7 eV , indicating that our microcalorimeter spectrometer has a Gaussian instrument response. The other heat pulse resolutions from the AlGaAs data set are $8.5 \pm 0.3\text{ eV}$ (FWHM) at 778 eV and $8.7 \pm 0.3\text{ eV}$ (FWHM) at 1840 eV . As will be shown below, these heat pulse resolutions are consistent with the energy resolution obtained from an analysis of AlGaAs and Al spectra from the AlGaAs data set.

To investigate the energy resolution as a function of energy, a series of heat pulse spectra over a large energy range were acquired as part of the multiple element data set previously used to determine the energy nonlinearity of the microcalorimeter. The energy-corrected heat pulse spectra were fitted using Gaussian curves to obtain the heat pulse energy resolution (FWHM) at different energies, as shown

in Fig. 21. The energy resolution obtained with this multiple element data set does not represent the best energy resolution obtained with our microcalorimeter spectrometer mounted on the SEM, but rather the typical energy resolution that can be achieved for real-time spectrum acquisition using analog pulse processing and a multichannel analyser. To cover the large energy range with the available 4096 channels of the multichannel analyser required the use of energy binwidths on the order of 2 eV per channel at low energies, increasing to over 4 eV per channel at the highest energies owing to the energy nonlinearity of the microcalorimeter. As described previously, these large energy binwidths (relative to the microcalorimeter energy resolution) contribute to the predicted energy resolution degradation for real-time analog processing and provide an explanation for the steady rise in the energy resolution at the higher energies. The observed heat pulse energy resolution of $14.1 \pm 0.4\text{ eV}$ at 5.6 keV is larger than the predicted energy resolution of $\approx 10\text{ eV}$ at 6 keV owing to nonoptimal detector biasing and additional noise sources such as ground loops and field noise.

X-ray spectra from several technologically important materials were also analysed to determine the instrument-response energy resolution. Compared with the direct determination of energy resolution from heat pulse spectra, the analysis of acquired X-ray spectra is complicated by the natural linewidths of X-ray lines, which are well described by a Lorentzian line shape. Lorentzian peaks are characterized by narrow FWHM widths and long tails. Typical natural linewidths range from less than 1 eV FWHM for low-Z $K\alpha$ lines to over 10 eV FWHM for high-Z K, L and M lines. Because these natural linewidths can be comparable to the energy resolution of our microcalorimeter, it is necessary to fit measured X-ray peaks to a convolution of the Lorentzian natural line shape with the Gaussian instrument response function. The resulting peak shape function, known as a Voigt function, cannot be expressed in analytical form and must be evaluated either numerically or by using a series approximation.

In order to obtain detailed fits to experimental data, it is also necessary to include the effect of X-ray satellite lines. X-ray satellite lines result from transitions in atoms with multiply (usually doubly) ionized inner shells, typically leading to a series of lines on the high-energy side of a parent X-ray line. Doubly ionized atoms can result from an electron beam directly knocking out two inner shell electrons or knocking out just one, with a subsequent emission of an Auger electron. The number, position, linewidth and relative weighting of satellite peaks with respect to main peaks can depend on several factors including Z, Auger transition probabilities, chemical bonding state and beam voltage (Hirsh, 1942; Fisher & Baun, 1965; Agarwal, 1991).

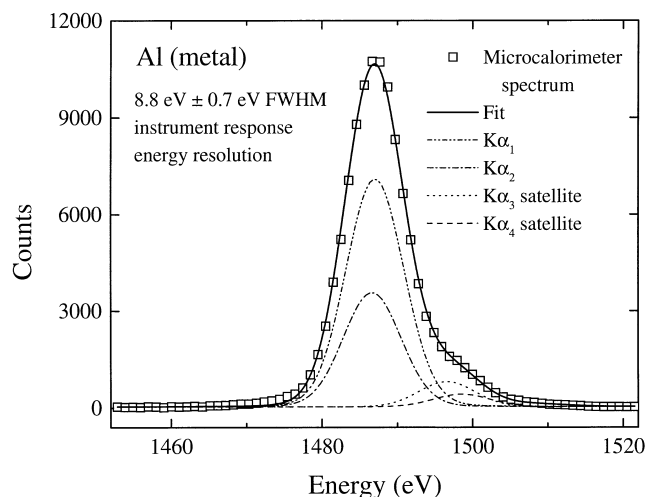


Fig. 22. Microcalorimeter spectrum of Al metal (open squares), previously shown in Fig. 18. Also shown is a fit to the data of the Gaussian instrument-response energy resolution convolved with the reported natural linewidths of the X-ray lines, yielding an instrument-response energy resolution of 8.8 ± 0.7 eV FWHM. The energies, natural linewidths and relative weightings of Al (metal) $K\alpha_{1,2}$ and satellite lines used in this fit are discussed in the text. In addition to the Al (metal) $K\alpha_{1,2}$ peaks and $K\alpha_{3,4}$ satellites shown, lower-intensity $K\alpha'$, $K\alpha_5$ and $K\alpha_6$ satellites were included in the fit but are not plotted, for clarity. The fit deviates from the data at energies near 1470 eV, which corresponds to the position of the collimation artefact previously shown in Fig. 18. Including a Gaussian peak at this energy significantly improved the fit (not shown), yielding an instrument-response energy resolution of 8.7 ± 0.3 eV FWHM.

An Al spectrum with a prominent high-energy shoulder caused by unresolved satellite lines is shown in Fig. 22. This spectrum was previously described and presented in Fig. 18, and was obtained as part of the AlGaAs data set. A fit to the data of the Gaussian instrument-response energy resolution convolved with the reported natural linewidths of the X-ray lines is also shown, in which the energies, natural linewidths and relative weightings of Al (metal) $K\alpha_{1,2}$ and satellite lines have been obtained from the literature, as will be described below. This nonlinear fit yields a Gaussian instrument-response energy resolution of 8.8 ± 0.7 eV FWHM, which is consistent with the previously determined heat pulse resolutions for the AlGaAs data set of 8.7 ± 0.1 eV FWHM at 1258.7 eV and 8.7 ± 0.3 eV FWHM at 1840 eV. The indicated uncertainty in the Gaussian instrument-response energy resolution includes both the statistical uncertainty and an estimate of the uncertainty inherent in the assumed natural linewidths and satellite weightings. The Al $K\alpha_{1,2}$ lines at 1486.9 and 1486.5 eV were fitted to true Voigt functions using semiempirical Al $K\alpha_{1,2}$ Lorentzian natural linewidths of 0.43 eV FWHM (Krause & Oliver, 1979). Reported Al satellite natural linewidths were not found, so Al metal

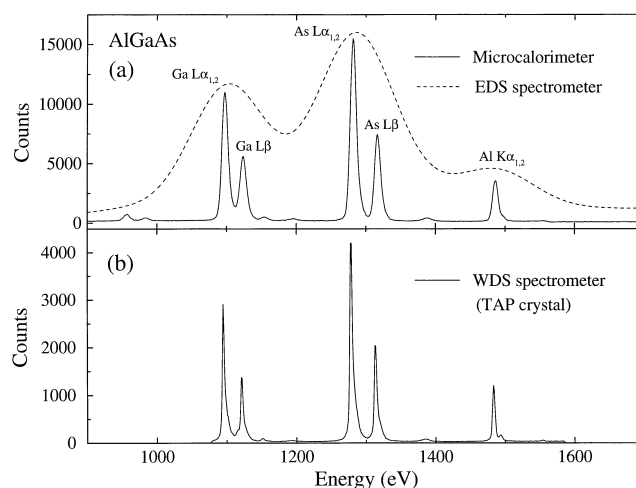


Fig. 23. (a) Microcalorimeter spectrum of AlGaAs (solid line), previously presented in Figs. 9, 11 and 12. For comparison, an EDS spectrum is also shown. (b) WDS spectrum of AlGaAs. The original WDS wavelength spectrum consisted of 1024 points covering the energy range 1078–1585 eV, and was acquired at a scan rate of 2 s per point using a thallium acid phthalate (TAP) crystal under the following conditions: 5 keV beam voltage, 100 nA beam current, total time 2048 s, X-ray takeoff angle of 40° and a total of 95 376 counts. The wavelength spectrum was then converted to an EDS energy scale and rebinned using an energy binwidth of 1 eV per channel. Close correspondence between the microcalorimeter and WDS spectra is observed.

satellite lines including $K\alpha'$ (1492.3 eV), $K\alpha_3$ (1496.4 eV), $K\alpha_4$ (1498.4 eV), $K\alpha_5$ (1506.7 eV) and $K\alpha_6$ (1510.2 eV) were fitted using Gaussian peaks, with reported Al (metal) satellite peak intensity ratios (Nordfors, 1955; Fisher & Baun, 1965) used as constraints.

An improved fit yielding an instrument-response energy resolution of 8.7 ± 0.3 eV FWHM was obtained by including a Gaussian peak at 1470 eV, corresponding to the position of the collimation artefact shown in Fig. 18. The improved fit indicates that the collimation artefact, although significantly reduced by adjusting the electron beam position (to optimize the shadowing of the TES by the Si grid supporting the outer vacuum window, as described previously), was not entirely eliminated in this data set. In the future, better collimation will ensure that this (already reduced) artefact is completely eliminated.

For this fit, we found that it was necessary to use satellite parameters appropriate for Al metal instead of Al oxide in order to obtain a detailed fit to the data. Because the L shell energy levels associated with Al satellite transitions are affected by chemical bonding, the relative satellite weighting and satellite energies are different for Al metal and Al oxide (Nordfors, 1955; Fisher & Baun, 1965). Chemical bonding effects are even greater for light element X-ray lines such as the C $K\alpha$ line, in which significant peak shape changes and peak shifts on the order of 4 eV are observed for different

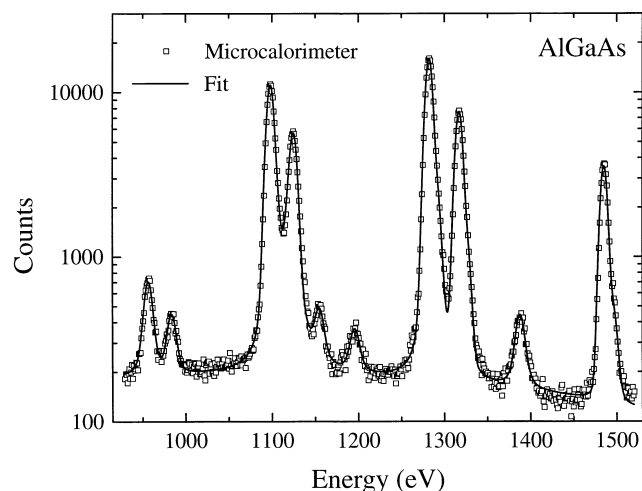


Fig. 24. Fit to the microcalorimeter AlGaAs spectrum shown in Fig. 23(a) of the Gaussian instrument-response energy resolution convolved with reported natural linewidths of the Al-K, Ga-L, As-L and selected satellite X-ray lines. Details of the fit are discussed in the text, and no matrix corrections were calculated. Good agreement is observed between the fit and the data, which are plotted on a logarithmic scale. The global fit yields a Gaussian instrument-response energy resolution of 9.3 ± 0.5 eV FWHM, compared with a heat pulse energy resolution of 8.8 ± 0.3 eV FWHM at 1487 eV.

oxidation states. Work is in progress to look for the effects of chemical bonding in such materials as C, S and Fe, which will become easier to observe as the energy resolution of the microcalorimeter is improved.

An AlGaAs spectrum was also analysed to obtain the instrument-response energy resolution. This spectrum, described and presented in Figs. 9, 11 and 12, was acquired as part of the AlGaAs data set and is shown in Fig. 23(a). For comparison, Figs. 23(a) and 23(b) also show spectra from identical samples obtained using a commercial Si(Li) ED spectrometer and a WD spectrometer.

Unlike the Si(Li) ED spectrometer, both our microcalorimeter spectrometer and the WD spectrometer have sufficient energy resolution to resolve most of the Al-K, Ga-L, and As-L X-ray peaks. Figure 24 shows a fit to the AlGaAs microcalorimeter spectrum of the Gaussian instrument-response energy resolution convolved with the reported natural linewidths of the X-ray lines, in which the energies, natural linewidths and relative weightings of X-ray lines have been obtained from the literature (Krause & Oliver, 1979; Fiori *et al.*, 1991; Perkins *et al.*, 1991; Campbell & Papp, 1995). Because matrix corrections were not calculated, as would be required in a detailed fit to account for significant differential absorption effects, many of the relative weightings of the X-ray lines within families are not constrained in this fit. A particular problem in the fit is constraining the relative weighting of the unresolved As L ℓ peak (at 1120 eV, with a natural linewidth of ≈ 12 eV), for

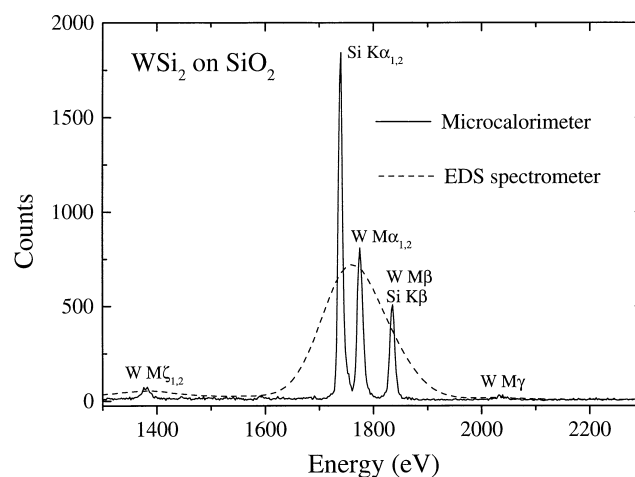


Fig. 25. Microcalorimeter spectrum of WSi₂, acquired under the following conditions: 10 keV beam voltage, 25.6 nA beam current, input count rate of 180 ± 20 s⁻¹, output count rate of 130 ± 10 s⁻¹, dead time of $28 \pm 5\%$, live time 200 s, specimen-detector distance of 37 ± 2 mm, and a total of 34 511 counts. This spectrum was acquired using a thin (≈ 100 nm) WSi₂ film on SiO₂ as part of the multiple element data set, and has been corrected for energy nonlinearity. The energy binwidth per channel varies from 2.1 to 2.4 eV over the energy range 1300–2300 eV. Also shown for comparison is an EDS spectrum of WSi₂.

which an approximate matrix correction calculation was needed. The continuum background is fitted to a quadratic polynomial, and only selected satellite lines are included in the fit. The global fit to the AlGaAs spectrum yields an average Gaussian instrument-response energy resolution of 9.3 ± 0.5 eV FWHM, which is slightly worse than the independently measured instrument-response energy resolution of 8.8 ± 0.3 eV FWHM at the higher energy of 1487 eV, as previously determined using heat pulses. The reported AlGaAs energy resolution uncertainty is dominated by the uncertainty in the assumed natural linewidths, background and the exclusion of satellite peaks. The difference between the heat pulse and fitted energy resolutions may have resulted from long-term temperature drift in the temperature control circuit, as this AlGaAs spectrum was acquired over 6000 s, as opposed to 1000 s for the Al spectrum also obtained as part of the AlGaAs data set.

The effect of natural linewidths in acquired spectra can be observed in the WSi₂ spectrum shown in Figs. 25 and 26, in which the widths of the W M $\alpha_{1,2}$ peaks at 1774.4 eV and the W M β peak at 1834.9 eV are greater than the width of the Si K $\alpha_{1,2}$ peak at 1740 eV. WSi₂ is an important interconnect material in semiconductor processing, with a peak overlap that cannot be resolved using semiconductor ED spectrometers. A fit to the spectrum of the Gaussian instrument response convolved with the Lorentzian natural linewidths is also shown in Fig. 26, assuming Si K $\alpha_{1,2}$

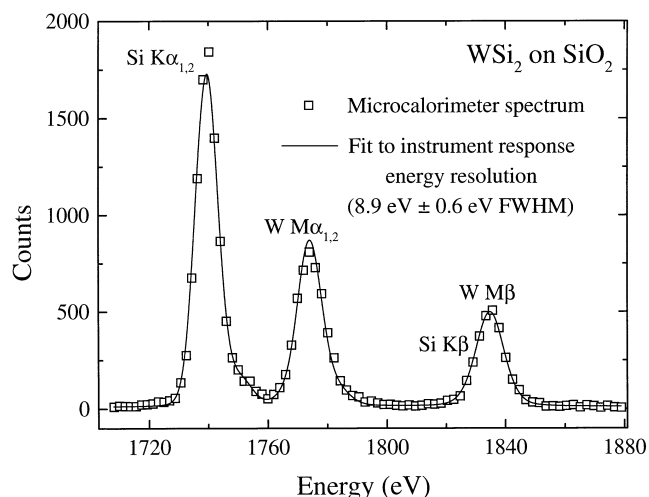


Fig. 26. Fit to the microcalorimeter WSi_2 spectrum shown in Fig. 25 of the Gaussian instrument-response energy resolution convolved with reported natural linewidths of the $\text{Si K}\alpha_{1,2}$, $\text{W M}\alpha_{1,2}$, $\text{W M}\beta$, and selected satellite X-ray lines. Details of the fit are discussed in the text, and no matrix corrections were calculated. The fit yields a Gaussian instrument-response energy resolution of 8.9 ± 0.6 eV FWHM, consistent with a heat pulse energy resolution of 9.0 ± 0.3 eV FWHM at 1794 eV.

natural linewidths of 0.49 eV (at 1740.0 eV and 1739.4 eV, respectively) and $\text{W M}\alpha_{1,2}$ and $\text{W M}\beta$ natural linewidths of 1.8 eV and 2.6 eV, respectively (Graeffe *et al.*, 1977; Krause & Oliver, 1979; Campbell & Papp, 1995). Fully constrained Gaussian peaks at 1746.3, 1750.7, 1753.1 and 1765.3 eV (Si-K satellite lines), and 1781.1 and 1841.6 eV (effective W-M satellite lines) were also included in the fit. No matrix corrections were attempted, and a constant background was assumed. The fit yields a Gaussian instrument-response energy resolution of 8.9 ± 0.6 eV FWHM, consistent with a heat pulse energy resolution of 9.0 ± 0.3 eV FWHM at 1794 eV also obtained in the multiple element data set.

Like WSi_2 , BaTiO_3 is a technologically important material with peak overlaps that cannot be resolved using a semiconductor ED spectrometer. A spectrum of a BaTiO_3 crystal, previously shown in Fig. 19, is expanded in Fig. 27 to show the almost completely resolved $\text{Ba L}\alpha$ and $\text{Ti K}\alpha$ peaks. The individual $\text{Ba L}\alpha_1$ (4465 eV) and $\text{L}\alpha_2$ (4450 eV) peaks and the $\text{Ti K}\alpha_1$ (4510 eV) and $\text{K}\alpha_2$ (4504 eV) peaks are not resolved, although the $\text{Ba L}\alpha_2$ peak is seen as a low-energy shoulder to the $\text{L}\alpha_1$ peak. Figure 28 shows a fit to the microcalorimeter spectrum of the Gaussian instrument response convolved with the natural linewidths of the $\text{Ba L}\alpha_{1,2}$ and $\text{Ti K}\alpha_{1,2}$ X-ray lines. In this fit, we assume $\text{Ba L}\alpha_{1,2}$ natural linewidths of 3.5 eV (Campbell & Papp, 1995), a $\text{Ti K}\alpha_1$ linewidth of 1.16 eV and a $\text{Ti K}\alpha_2$ linewidth of 1.18 eV (Krause & Oliver, 1979). The fit also includes fully constrained Gaussian peaks corresponding to $\text{Ba L}\alpha_3$ (4470.8 eV), $\text{Ba L}\alpha_5$ (4486.2 eV) and $\text{Ba L}\alpha_6$ (4491.0 eV)

satellites. No matrix corrections are attempted, and a constant background is assumed. The fit to the data yields an energy resolution of 11.3 ± 0.4 eV FWHM, consistent with a heat pulse energy resolution of 11.7 ± 0.3 eV FWHM at 4567 eV also obtained in this multiple element data set.

In the previous examples, we have made detailed fits to experimental spectra in order to determine the Gaussian instrument-response energy resolution as a function of energy, which is consistent with the energy resolution independently measured using heat pulses. The demonstrated agreement between X-ray and heat pulse energy resolutions is extremely important, as the independent determination of the Gaussian instrument response allows more information to be extracted from acquired X-ray spectra. In addition, the demonstrated ability to achieve detailed fits to TES microcalorimeter spectra may depend on the use of normal-metal absorbers with excellent X-ray thermalization properties and should not be assumed for other microcalorimeters.

Discussion: spectrometer comparison

To understand the potential impact of our microcalorimeter spectrometer for X-ray microanalysis, it is useful to consider the relative advantages and disadvantages of WD, ED and microcalorimeter spectrometers for quantitative and qualitative X-ray microanalysis. After a brief discussion of operating principles and experimental considerations, we will compare the spectrometers with respect to energy resolution, maximum count rate and X-ray collection efficiency. Although these comparisons are relevant to other X-ray analytical techniques such as X-ray fluorescence (XRF), we will restrict this discussion to electron-beam excitation techniques.

As described in the introduction, WD spectrometers are based on Bragg diffraction from carefully prepared and orientated crystals. To cover the desired X-ray energy range (100 eV to 12 keV), a WD spectrometer must satisfy the Bragg condition over a wide range of angles while maintaining the same X-ray emission (take-off) angle over the entire diffraction angle range. This geometrical constraint is solved using the fully focusing Johannson geometry, in which a precision mechanical system moves the diffraction crystal and the gas-flow proportional counter detector along a focusing circle of radius R , whose circumference is rocked about a point centred on the beam impact position on the specimen (Goldstein *et al.*, 1992). The crystal is bent to a radius of curvature of $2R$, and the surface of the crystal can be ground to a radius of curvature of R in order to maximize the solid angle of collection (variable, ≈ 0.01 sr) of the WD spectrometer. Even with this critical geometric solution, the energy range covered by the selected d -spacing of a single crystal is limited. Acquiring a complete X-ray spectrum requires the

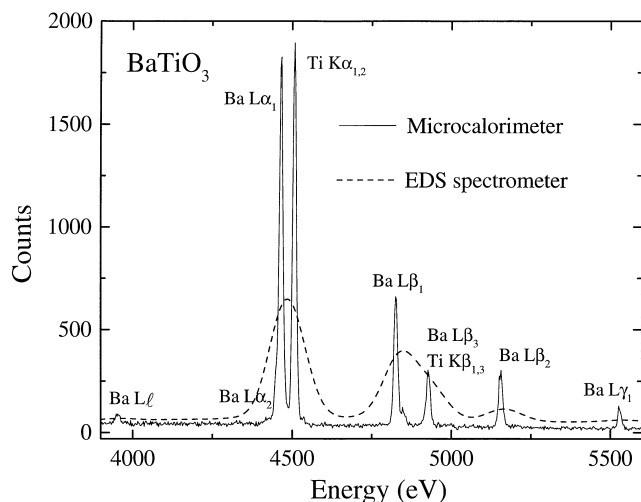


Fig. 27. Microcalorimeter spectrum of BaTiO_3 , previously presented in Fig. 19. Also shown for comparison is an EDS spectrum of BaTiO_3 .

use of multiple crystals, which are often mounted on a turret to bring a selected crystal onto the diffraction circle. For example, the energy range from 100 eV to 12 keV can be covered using a four-crystal turret with a layered synthetic material (LSM, 0.1–0.55 keV), thallium acid phthalate (TAP, 0.5–2.4 keV), pentaerythritol (PET, 1.5–5.5 keV) and lithium fluoride (LiF, 3.3–12 keV) crystals.

The narrow 'rocking curve' characteristic of X-ray diffraction is responsible for both the excellent energy resolution (≈ 20 eV at 6 keV, see Fig. 29) and many of the operational difficulties associated with WD spectrometers. One consequence of the narrow rocking curve is that precise mechanical motions for peak finding and resetting are required for reproducibility, particularly when a sequence of elemental peaks is measured under automated control. The narrow rocking curve also results in a limited focusing volume for the WD spectrometer. The focusing volume is an ellipsoid with the longest axis (of millimetre length) parallel to the width of the diffraction crystal, but with very short axes (of micrometre length) perpendicular to the diffracting planes and perpendicular to the crystal axis of bending. The volume of the specimen that is excited by the electron beam (with typical linear dimensions ranging from 0.5 to 5 μm) must be reproducibly positioned within this focus ellipsoid with the aid of a light microscope having a fixed position and a narrow depth of focus (± 2 μm or less) which is centred on the coincident focus position of the WDS and the electron beam column axis.

The WD spectrometer provides the analyst with practical analytical X-ray spectrometry with sufficient resolution to separate most spectral interferences. Owing to the inherently short dead time of the gas-filled proportional counter (≈ 2 μs), the WD spectrometer has a maximum count rate of 50 000 s^{-1} or higher for the channel selected by Bragg

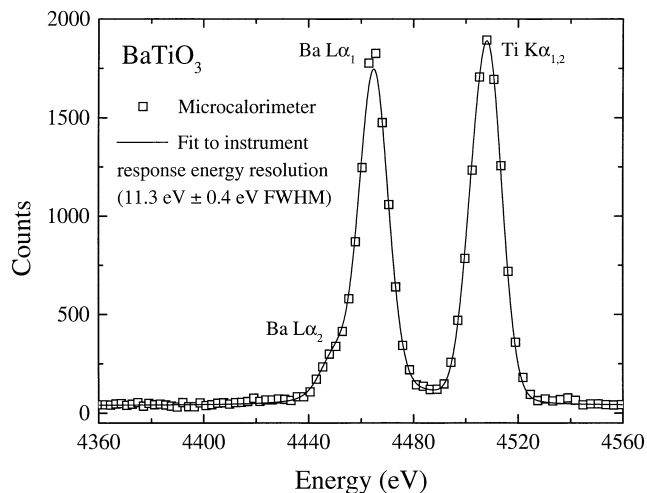


Fig. 28. Fit to the microcalorimeter spectrum of BaTiO_3 of the Gaussian instrument-response energy resolution convolved with reported natural linewidths of the $\text{Ba L}\alpha_{1,2}$, $\text{Ti K}\alpha_{1,2}$ and selected satellite X-ray lines. Details of the fit are discussed in the text, and no matrix corrections were calculated. The fit yields an energy resolution of 11.3 ± 0.4 eV FWHM, consistent with a heat pulse energy resolution of 11.7 ± 0.3 eV FWHM at 4567 eV.

diffraction. To achieve these large count rates, high beam currents (typically 1 nA to 1 μA) must be used to compensate for the low quantum and geometrical collection efficiency of WD spectrometers. With such high beam currents, a WDS system can provide practical analysis in reasonable time periods, especially when multiple WD spectrometers are incorporated for simultaneous peak measurement under computer automation.

The principal limitation of WD spectrometers for practical analysis is in qualitative analysis, that is, the identification of the constituents present in the analytical volume from their characteristic X-ray peaks. In WDS qualitative analysis, a complete spectrum is acquired by mechanically scanning through the entire range of each diffracting crystal. This process is slow, requiring up to 10 min or more per crystal depending on the level of minor and trace element detection desired. This time penalty generally precludes performing qualitative analysis at each specimen location when many separate points are to be measured. Real specimens are often heterogeneous on the microstructural scale, so not performing qualitative analysis at each location creates a significant possibility that important analytical information will be lost.

The introduction of semiconductor ED spectrometers sparked a rapid revolution in analytical X-ray spectrometry. The semiconductor ED spectrometer provides a simple line-of-sight installation and a reasonably large solid angle (up to 0.25 sr) with minimal physical size (snout diameter 2 cm). There is no need for mechanical motion during spectral measurement. The energy resolution (≈ 130 eV at 6 keV; see Fig. 29) is much poorer than that obtained with

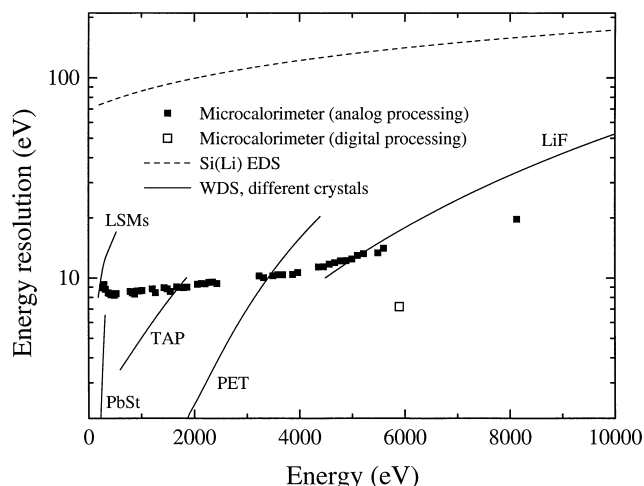


Fig. 29. Energy resolution vs. energy for semiconductor ED, WD and microcalorimeter spectrometers, after Reed (1995) and Heinrich (1981). The uncertainty in the measured energy resolutions for the microcalorimeter (using analog and digital processing) is given by the size of the data points. The Si(Li) EDS energy resolution is 140 eV at 5.9 keV, and the WDS crystals are lithium fluoride (LiF), pentaerythritol (PET), thallium acid phthalate (TAP), lead stearate (PbSt) and layered synthetic materials (LSMs).

WD spectrometers, and the count rate is limited to $\approx 3000 \text{ s}^{-1}$ in the highest resolution mode (using the longest pulse-shaping time constants). The dead time is paralyzable, and the EDS detector must view the full spectrum without any of the filtering that occurs with diffraction in the WD spectrometer. However, this continual view of the entire excited X-ray spectrum (100 eV to 25 keV for Si(Li) detectors; 100 eV to 100 keV for HPGe detectors) is the single greatest contribution of the ED spectrometer to practical analysis. Because the complete X-ray spectrum is always obtained from every position measured on the specimen, qualitative analysis can (and should) be performed on each spectrum so that the heterogeneous character of the specimen immediately becomes obvious.

As a result of the utility of EDS spectral coverage, as well as the long-term stability and ease of operation in computer-assisted systems, the semiconductor ED spectrometer has developed enormous popularity and has almost completely displaced the WD spectrometer for SEM-based X-ray microanalysis. The main drawbacks to semiconductor EDS are the significant possibility that minor or trace constituents are not recognized due to peak interferences from major constituents and escape peaks, and the more modest limits of detection compared with WD spectrometers, due to poorer peak-to-background ratios. In fact, WD and semiconductor ED spectrometers are highly complementary in combined use, with the strengths of one compensating for the weaknesses of the other, although the complications

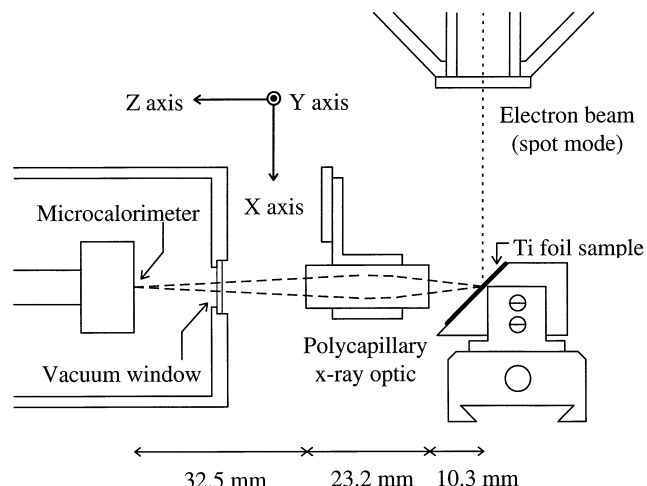


Fig. 30. Diagram (approximately to scale) of microcalorimeter, polycapillary X-ray optic and Ti foil sample inside the SEM chamber. The polycapillary optic had an input capture angle of 13.4° , input focal spot width of $\approx 100 \mu\text{m}$ (FWHM), output convergent angle of 5.7° and an output focal spot width of $\approx 380 \mu\text{m}$ (FWHM). Translation stages and microcalorimeter heat shields are not shown for clarity.

and expense of incorporating the WD spectrometer are such that only a small fraction of SEMs are so equipped.

We now turn to the potential role of the microcalorimeter spectrometer in X-ray microanalysis, which will be determined by its relative performance and ease of use with respect to the already established EDS and WDS techniques. After comparing the energy resolution, solid area and count rate of the different spectrometers, we will examine the relative utility of the microcalorimeter for certain critical applications using figures of merit based on combinations of these parameters.

The strong interest in developing microcalorimeters for X-ray microanalysis is due to their excellent energy resolution and EDS mode of operation. As shown in Fig. 29, the energy resolution of our microcalorimeter spectrometer corresponds to an order-of-magnitude improvement over semiconductor ED spectrometers and rivals that of WD spectrometers. The energy resolution of the microcalorimeter is not a strong function of energy compared with the strongly varying WDS energy resolution. With theoretical energy resolution limits near 1 eV, the microcalorimeter has the potential to well surpass WD spectrometers in energy resolution.

The true Gaussian instrument response function of our normal-metal-absorber TES microcalorimeter allows simpler spectrum modelling and analysis than that for WDS spectra, which are difficult to fit because the WDS instrument response function changes dramatically (and unpredictably) with energy and diffraction crystal (ranging from near Gaussian for layered synthetic materials (LSMs)

to strongly Lorentzian for lithium fluoride (LiF), as discussed in Goldstein *et al.*, 1992). In WDS analysis, better energy resolution is sometimes viewed as a liability because of the resulting difficulty in reproducibly determining peak positions and the increased sensitivity to polarization effects and peak shifts and distortions due to chemical bonding effects. For example, LSMs with improved X-ray reflection efficiencies are preferred over lead stearate (PbSt) crystals for low X-ray energy analysis (Bastin & Heijligers, 1991), even though PbSt has much better energy resolution, as shown in Fig. 29. The microcalorimeter, on the other hand, is not sensitive to the polarization of incident X-rays. Because the microcalorimeter naturally allows spectral analysis by peak integration (as opposed to the peak height analysis at a single wavelength commonly used for WDS), improved energy resolution is always desirable, particularly for the analysis of materials in which chemical bonding effects are important.

In a comparison of count rates, the WD spectrometer is clearly superior, with count rates of greater than $50\,000\text{ s}^{-1}$ possible without degradation in energy resolution. Although semiconductor ED spectrometers can operate at count rates greater than $10\,000\text{ s}^{-1}$, high-resolution semiconductor EDS is limited to count rates of $\approx 3000\text{ s}^{-1}$. While the output count rate of the microcalorimeter (currently about 150 s^{-1}) is much lower than WDS and EDS count rates, the microcalorimeter devices tested so far have not yet been optimized for speed. We are confident that the microcalorimeter output count rate can be increased to at least $500\text{--}1000\text{ s}^{-1}$ without degradation of energy resolution. Additionally, an array of microcalorimeters could be used to increase the effective count rate significantly.

Next, we compare the different spectrometers with respect to geometrical collection efficiency, which is expressed as a solid angle of collection. Semiconductor EDS detectors are available with areas as large as 60 mm^2 and can be placed as close as 15 mm to the specimen, resulting in a solid angle of 0.270 sr (270 msr). High-resolution EDS detectors with areas of 10 mm^2 and specimen–detector distances of 20 mm have much smaller solid angles, $\approx 25\text{ msr}$. The solid angle of WD spectrometers varies from 8 msr to 25 msr as a function of energy for each diffraction crystal (Reed, 1995). The relatively large solid angle of WD spectrometers is somewhat misleading, however, because only X-rays of a narrow energy band are accepted for measurement, effectively reducing the collection efficiency by up to several orders of magnitude. In comparison, microcalorimeters have typical absorber areas of 0.06 mm^2 , which corresponds to a solid angle of 0.05 msr at a sample–detector distance of 35 mm.

Although the solid angle of the microcalorimeter is small, the geometrical collection efficiency can be increased in several ways. Because the use of electrothermal feedback in

our microcalorimeters provides a larger heat capacity budget than that of other microcalorimeters, in principle it is possible (although technically challenging) to increase the normal-metal absorber area to greater than 1 mm^2 without loss of energy resolution. Another method to increase the effective area (and effective count rate) is to use an array of microcalorimeters.

The geometrical collection efficiency of the microcalorimeter spectrometer can also be increased with the use of an X-ray lens. One such X-ray lens is a polycapillary X-ray optic (Kumakhov & Komarov, 1990) consisting of tens of thousands of fused glass capillaries, which efficiently deflect X-rays of a wide energy range over large angles by means of multiple grazing-incidence reflections. The optic is shaped in such a way that all capillaries are directed toward common focal points at both input and output ends. Electron-beam-excited X-rays from a small specimen volume are collected over a large solid angle and focused onto the small-area absorber of the microcalorimeter.

In a preliminary experiment (Wollman *et al.*, 1997b), a polycapillary X-ray optic was placed between our microcalorimeter spectrometer and a Ti foil specimen in an SEM, as shown in Fig. 30. We used translation stages to align the optic to maximize the X-ray transmission. With the SEM in spot mode, X-ray spectra were acquired at different positions across the input focal spot of the optic. The high- and low-energy gain of the optic was determined at each position from the ratio of peak areas for the Ti K- and L-family characteristic X-ray peaks (with the bremsstrahlung background subtracted) acquired with and without the optic, at a fixed sample-to-detector distance of 66 mm. Figure 31 shows the decrease in the high- and low-energy gain as the electron beam was moved away from the centre of the input focal spot. The ratio of the high- and low-energy optic gain is largely independent of beam position. Further experiments are planned to characterize fully (channel by channel) the spectral transmission of the optic as a function of energy.

The measured optic gain of ≈ 300 corresponds to an increase in the effective area of the microcalorimeter from 0.06 mm^2 to almost 5 mm^2 , referred to a typical specimen–detector distance of 35 mm without the optic in place. This effective area corresponds to a solid angle of 4 msr , which is competitive with typical solid angles of WD and high-resolution ED spectrometers.

A more useful measure of X-ray collection ability is the collection efficiency, which we define as the product of the geometrical solid angle and the overall spectrometer efficiency at an energy of 1.7 keV . This energy corresponds to the Si $K\alpha$ X-ray line, which is chosen as a compromise between the Mn $K\alpha$ X-ray line at 5.9 keV (typically used to specify energy resolution) and important light-element X-ray lines at energies below 1 keV . Specifying the spectrometer efficiency at this energy allows us to avoid the

Table 1. Comparison of different X-ray spectrometers using the most important detector parameters: energy resolution (FWHM), maximum count rate, solid angle, and collection efficiency. Here we have defined the collection efficiency as the product of the solid angle and the overall spectrometer efficiency (at Si K α , 1.7 keV) to provide a more useful measure of X-ray collection ability. The large-area and high-resolution EDS parameters are for 60 mm² and 10 mm² detectors, respectively, at a specimen–detector distance of 20 mm. The WDS parameters are for a typical analytical spectrometer with multiple crystals. The parameters for the remaining low-temperature detectors assume a 35 mm specimen–sample distance and a count rate that is estimated, where appropriate, from signal fall times. Note that the collection efficiency for all of the low-temperature detectors can be improved with polycapillary optics to a similar extent as for our TES microcalorimeter.

Spectrometer type	Energy resolution (eV)	Maximum count rate (s ⁻¹)	Solid angle (msr)	Collection efficiency (msr)
EDS (large-area)	175 (at 6 keV)	30000	150	115
	145 (at 6 keV)	5000	150	115
EDS (high-resolution)	130 (at 6 keV)	3000	25	19
WDS	2–20	50000	8–25	0.8–2.5*
Semiconductor microcalorimeter	7–8	100	0.07	0.04
SIS tunnel junction	29 (at 6 keV)	2500	0.01	0.005
NIS microcalorimeter	18–30	2500	0.2	0.1
TES microcalorimeter	7–8	150	0.05	0.03
TES microcalorimeter with polycapillary optics	7–8	150	4	2

* Because a WDS spectrometer only accepts X-rays of a narrow energy band, its practical collection efficiency is further reduced (up to several orders of magnitude) when scanned over the entire energy range.

differences in the low-energy X-ray transmission of different types of vacuum windows and also accounts for the additional X-ray attenuation of the Al IR-blocking filters of our microcalorimeter spectrometer compared with semiconductor ED spectrometers. The overall spectrometer efficiency of our TES microcalorimeter spectrometer as a function of energy was presented in a previous section (see Fig. 13) and has a calculated value of 0.56 at 1.7 keV. The resulting collection efficiency for the combination of our microcalorimeter and the polycapillary optic is 2 msr, which is larger than the WDS collection efficiency of ≈ 1 msr, and only a factor of 10 smaller than the high-resolution semiconductor EDS collection efficiency of 19 msr.

A direct comparison of the energy resolution, maximum count rate, solid angle and collection efficiency of the different spectrometers is presented in Table 1. The table also includes parameters from other competing low-temperature EDS detectors such as superconductor–insulator–superconductor (SIS) tunnel junctions (Mears *et al.*, 1996), and semiconductor-based (McCammon *et al.*, 1991; Silver *et al.*, 1996) and normal–insulator–superconductor (NIS) microcalorimeters (Nahum & Martinis, 1995).

At first consideration, our microcalorimeter X-ray spectrometer appears to have the characteristics of an ‘ideal’ spectrometer. The examples of spectra shown here illustrate the utility of the high energy resolution of the microcalorimeter X-ray spectrometer to resolve peak interferences, a classic task for WD spectrometers. The energy-

dispersive character of the microcalorimeter gives immediate access to the complete X-ray spectrum for critical qualitative and quantitative analysis, the classic strength of ED spectrometers. When coupled with a polycapillary optic, the microcalorimeter has a collection efficiency larger than that of WD spectrometers and competitive with that of high-resolution ED spectrometers. While the maximum count rate of the microcalorimeter is currently ≈ 150 s⁻¹, we are confident that this can be improved to at least 500–1000 s⁻¹ in the near future, competitive with the maximum count rate of high-resolution semiconductor ED spectrometers.

In the preceding discussion, we have compared spectrometer performance in terms of important basic parameters without considering their relationship to practical analysis in specific analytical situations. Successful analysis includes not only the determination of the qualitative and quantitative composition of a specimen, but also an estimate of the specimen heterogeneity and the uncertainty in the reported measurements. The analyst must be able to say with some degree of confidence that a trace element is either present or not present in the sample of interest. To provide this information, the sensitivity of the analytical technique, usually expressed as a mass detection limit, must be determined. In addition, microanalysis must be performed in a timely manner to be useful. Here the important factor is the speed of analysis, as determined by the amount of real time necessary to reach a desired limit of detection.

Practical operation for trace element detection requires both a high spectral peak-to-background ratio and a statistically sufficient number of measured peak X-ray counts above background. Statham (1995) has analysed the relationship between peak count rate R and spectrometer resolution (FWHM) for various analytical situations. For trace level measurements in the absence of peak interferences, Statham's figure of merit Q_1 provides a comparative measure of analysis speed and has the form

$$Q_1 = R/\text{FWHM}.$$

To consider a specific example, R is $\approx 10\,000\text{ s}^{-1}$ and $\text{FWHM} = 140\text{ eV}$ for trace detection of Mn in Fe using an Si(Li) ED spectrometer. For the microcalorimeter with an energy resolution of 10 eV, the same figure of merit can be achieved with a minimum count rate of 700 s^{-1} , which should be achievable in future microcalorimeter systems. For higher count rates, the microcalorimeter will be superior to the semiconductor ED spectrometer.

Statham (1995) also considers the relative importance of resolution and count rate for analysis in the presence of peak interferences. For trace level measurements assuming two unresolved peaks and a dominant background, Statham's figure of merit Q_3 has the form

$$Q_3 = R/\text{FWHM}^3.$$

Because this figure of merit is valid only for energy resolutions that are large enough to cause severe overlap, we cannot use it to compare the microcalorimeter and ED spectrometers directly. However, it shows the relative benefit of improved resolution over count rate for practical analysis in the presence of overlapping peaks. In this analytical situation, the microcalorimeter spectrometer already outperforms semiconductor ED spectrometers. A microcalorimeter spectrometer is even more compelling when there are more than two overlapping peaks to be analysed or if automatic peak identification is desired, because the relevant figures of merit (Statham, 1995) are dominated by even higher powers of the energy resolution.

Since the WD and microcalorimeter spectrometer have similar energy resolution and therefore will achieve similar spectral peak-to-background ratios, the limits of detection should also be similar. Trace element detection with the WD spectrometer benefits greatly from the high maximum count rates coupled with the spectral filtering provided by diffraction. By progressively increasing the incident electron beam current to the microampere range, as can be achieved with thermal emission sources, high count rates are obtained exclusively from the trace peak of interest, while X-rays from the major constituent peaks are prevented from reaching the WDS detector. In contrast, with its paralysable dead time and unrestricted view of the complete X-ray spectrum, the microcalorimeter inevitably spends most of the available time detecting the abundant X-rays produced by the major constituents. The live time is effectively

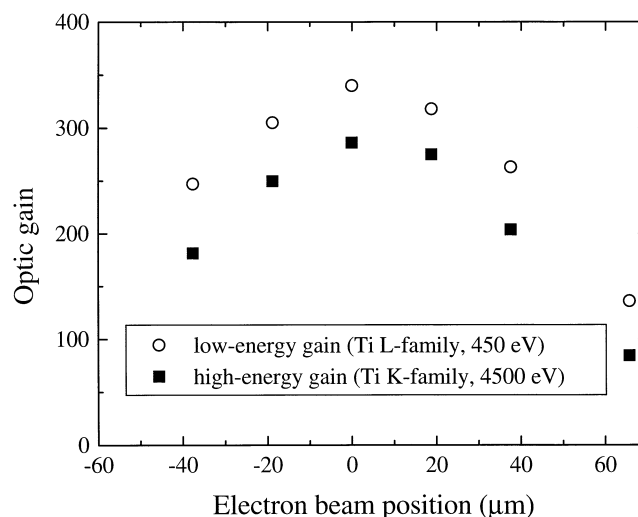


Fig. 31. High- and low-energy gain of the polycapillary optic as a function of electron beam position. The beam position was varied along the 45° slope of the sample, so that the input focal spot of the optic was simultaneously scanned in two dimensions, X and Z. The electron beam position was measured in the plane of the sample surface. The uncertainty in the measured high- and low-energy optic gain is approximately $\pm 12\%$, and is dominated by the uncertainty in the amount of shadowing of the microcalorimeter by the Si grid supporting the thin polymer vacuum window.

partitioned among the constituents according to their X-ray production rate, which depends on abundance and the excitation efficiency. For X-ray peaks with similar excitation efficiencies, the mass fraction multiplied by the maximum count rate gives the total count rate available for the detection of a trace peak. Thus, at a mass fraction of 0.001, the trace element peak receives $\approx 0.1\%$ of the total count rate. The microcalorimeter will always be at a disadvantage compared with WD spectrometers for trace element work when only one peak is to be measured. However, the microcalorimeter can measure all trace elements at the same time with the same radiation dose. Thus, for complex multielement specimens, the microcalorimeter may gain an absolute advantage over WD spectrometers.

Potential applications

Several important microanalysis problems can be solved using the microcalorimeter. Although the energy resolution of the microcalorimeter spectrometer will be extremely useful for resolving peak interferences at all X-ray energies, the biggest impact on X-ray microanalysis will likely be at low X-ray energies. Here, the ability of our microcalorimeter spectrometer to resolve low-energy X-ray lines in complicated spectra will facilitate X-ray microanalysis at higher spatial resolution.

As the dimensions of features of interest in technology-intensive industries and materials research continue to

shrink to well below 1 μm , successful X-ray microanalysis at high spatial resolution becomes increasingly important for understanding critical materials issues. This high spatial resolution has traditionally been achieved for imaging using a transmission electron microscope (TEM) and thinned, small-area (0.01 mm^2) samples, but now can also be obtained with a field-emission-gun scanning electron microscope (FEG-SEM) operating at low beam energies. The advantage of a FEG-SEM is that traditional flat, polished samples can be characterized with high spatial resolution over much larger areas ($>100\text{ mm}^2$).

In addition to the high spatial resolution for imaging in an FEG-SEM, the low-energy electron beam (1–5 keV) reduces the X-ray generation volume in the sample to submicrometre dimensions. For example, the X-ray spatial resolution obtained with a 5-keV electron beam is $\approx 0.5\text{ }\mu\text{m}$ for Si and is reduced to $\approx 0.1\text{ }\mu\text{m}$ using a 2-keV electron beam. With these low beam energies, however, X-ray spectra can be acquired over only the limited energy range from 100 eV to a few keV, in which there are many peak interferences between K-lines of light elements, L-lines of transition elements and M-lines of heavy elements. This results in very complicated spectra that are difficult to analyse using the poor fractional energy resolution of semiconductor ED detectors in this energy range. Microcalorimeter spectrometers have the excellent energy resolution at low energies that is needed to resolve most of the overlapping X-ray peaks and unambiguously identify the elemental constituents.

In addition to good energy resolution, it is also necessary to have a high collection efficiency for successful high-spatial-resolution X-ray microanalysis. The small beam currents (0.1–1 nA) of both FEG-SEMs and TEMs result in inherently low X-ray production rates when used to image small mass-thickness targets such as nanoscale particles or thin films. In these analytical situations, intrinsic X-ray count rates are limited and high collection efficiency is necessary to make efficient measurements. With its excellent energy resolution and good collection efficiency, the combination of our microcalorimeter spectrometer and a polycapillary optic may provide the best detector solution for achieving the goal of practical X-ray microanalysis at high spatial resolution.

A critical opportunity for high-spatial-resolution X-ray microanalysis using the microcalorimeter spectrometer is the problem of identifying submicrometre contaminant particles *in situ* as they accumulate on semiconductor substrates during processing (SEMATECH, 1995; Silver *et al.*, 1996). In current defect review tools, light scattering systems rapidly survey a complete 200-mm-diameter wafer and locate rare particles with diameters as small as 50 nm. The substrate is then loaded into an FEG-SEM and the coordinates from the optical system are used to locate the suspect particle, which then must be identified using X-ray microanalysis.

There are several problems with the current use of semiconductor ED spectrometers for this application. Because semiconductor EDS detectors have such poor fractional energy resolution at low energies, for unambiguous identification of particle composition it is often necessary to examine the high-energy portion of the X-ray spectrum (5 keV to over 10 keV), in which the characteristic X-ray lines are more easily resolved. At high excitation energies, however, the large majority of X-rays are produced by electrons that pass through the small particle and interact in the substrate. If the beam energy is lowered to reduce the X-ray generation volume to the size of the nanoscale particle, it is difficult to identify particle constituents owing to the large number of overlapping peaks in complicated low-energy spectra, particularly when both low-Z and high-Z elements are present. In addition, the semiconductor EDS detector cannot resolve many of the severe peak interferences common to several important semiconductor device/interconnect materials, such as Ti-L and N-K lines in TiN, W-M and Si-K lines in WSi_2 , and O-K with the L-lines of V, Cr, Mn in metal alloys.

All of these problems will only get worse as the dimensions of semiconductor devices (and 'killer' defects) continue to shrink. With its excellent energy resolution at low X-ray energies and EDS mode of operation, the microcalorimeter spectrometer may be able to meet the increasingly critical need for improved particle identification in the semiconductor industry. The energy resolution of the microcalorimeter spectrometer is sufficient to resolve directly most of the peak interferences described above, allowing particle identification at higher X-ray spatial resolution using even lower beam energies. In addition, the energy resolution is typically sufficient to separate the characteristic peaks of an element from the absorption edges of that same element. For the semiconductor ED spectrometer, these two features are indistinguishable for low-energy photons, further complicating analysis.

For the identification of particles in which peak interferences are not as severe, it may be advantageous (based on figures of merit discussed previously) to use a microcalorimeter that is optimized for higher count rates but with an energy resolution on the order of 20–30 eV. It should be possible to fabricate a second TES microcalorimeter (or a different low-temperature detector with higher count rate such as the NIS microcalorimeter) on the same silicon nitride membrane as the primary high-energy-resolution TES microcalorimeter. In this case, the analyst could use the polycapillary optic to select the desired detector, depending on the analytical situation.

Conclusion

In this paper, we have characterized the TES microcalorimeter spectrometer system developed at NIST for use in

real-time X-ray microanalysis. Careful analysis of digitized X-ray pulses yields a baseline microcalorimeter instrument-response energy resolution of 7.2 ± 0.4 eV FWHM at 5.89 keV for Mn $K\alpha_{1,2}$ X-rays from a radioactive ^{55}Fe source. With the spectrometer mounted on an SEM, we have achieved a Gaussian instrument-response energy resolution for analog processing of better than 10 eV FWHM over a broad energy range at real-time output count rates up to 150 s^{-1} . The TES microcalorimeter spectrometer is a powerful instrument for X-ray microanalysis with the energy resolution of a WD spectrometer and the parallel energy detection of a conventional ED spectrometer. The TES microcalorimeter spectrometer may solve many important microanalysis problems, including high-spatial-resolution X-ray microanalysis at low energies (100 eV to a few keV), the resolving of overlapping X-ray lines in technologically important materials (such as BaTiO_3 , WSi_2 and TiN), and the identification of small contaminant particles important to the semiconductor industry.

References

- Agarwal, B.K. (1991) *X-Ray Spectroscopy*, 2nd edn. Springer-Verlag, New York.
- Bastin, G.F. & Heijligers, H.J.M. (1991) Quantitative electron probe microanalysis of ultra-light elements (boron-oxygen). *Electron Probe Quantitation* (ed. by K. F. J. Heinrich and D. E. Newbury), pp. 145–161. Plenum Press, New York.
- Campbell, J.L. & Papp, T. (1995) Atomic level widths for x-ray spectrometry. *X-Ray Spectrom.* **24**, 307–319.
- Castaing, R. (1951) *Application of Electron Probes to Local Chemical and Crystallographic Analysis*. Thesis, University of Paris.
- Fiori, C.E., Swyt, C.R. & Myklebust, R.L. (1991) *Standard Reference Data Base 36*, available from the Office of Standard Reference Data, National Institute of Standards and Technology, Gaithersburg, U.S.A.
- Fisher, D.W. & Baun, W.L. (1965) Diagram and nondiagram lines in K spectra of aluminum and oxygen from metallic and anodized aluminum. *J. Appl. Phys.* **36**, 534–537.
- Fitzgerald, R., Keil, K. & Heinrich, K.E.J. (1968) Solid-state energy-dispersive spectrometer for electron-microprobe x-ray microanalysis. *Science*, **159**, 528–529.
- de Gennes, P.G. (1964) Boundary effects in superconductors. *Rev. Mod. Phys.* **36**, 225–237.
- Goldstein, J.I., Newbury, D.E., Echlin, P., Joy, D.C., Romig, A.D. Jr, Lyman, C.E., Fiori, C. & Lifshin, E. (1992) *Scanning Electron Microscopy and X-ray Microanalysis*, 2nd edn. Plenum Press, New York.
- Graeffe, G., Juslen, H. & Karras, M. (1977) Si $K\alpha$ x-ray emission spectra of Si, SiC, SiO_2 , and Si_3N_4 . *J. Phys. B*, **10**, 3219–3227.
- Hagmann, C. & Richards, P. (1994) Two-stage magnetic refrigerator for astronomical applications with reservoir temperatures above 4 K. *Cryogenics*, **34**, 221–226.
- Heinrich, K.E.J. (1981) *Electron Beam X-ray Microanalysis*, pp. 125. Van Nostrand-Reinhold, New York.
- Hirsh, F.R. Jr (1942) A summary of x-ray satellites. *Rev. Mod. Phys.* **14**, 45–54.
- Irwin, K.D. (1995) An application of electrothermal feedback for high resolution cryogenic particle detection. *Appl. Phys. Lett.* **66**, 1998–2000.
- Irwin, K.D., Hilton, G.C., Wollman, D.A. & Martinis, J.M. (1996) X-ray detection using a superconducting transition-edge sensor microcalorimeter with electrothermal feedback. *Appl. Phys. Lett.* **69**, 1945–1947.
- Krause, M.O. (1979) Atomic radiative and radiationless yields for K and L shells. *J. Phys. Chem. Ref. Data*, **8**, 307–327.
- Krause, M.O. & Oliver, J.H. (1979) Natural widths of atomic K and L levels, $K\alpha$ x-ray lines and several KLL Auger lines. *J. Phys. Chem. Ref. Data*, **8**, 329–338.
- Kumakhov, M.A. & Komarov, E.F. (1990) Multiple reflection from surface x-ray optics. *Phys. Rep.* **191**, 289–350.
- Lee, P.L. & Salem, S.I. (1974) Widths and asymmetries of the $K\alpha_1$ and $K\alpha_2$ x-ray lines and the L_2 and L_3 fluorescence yields of the transition elements. *Phys. Rev. A*, **10**, 2027–2032.
- Lesyna, L., Di Marzio, D., Gottesman, S. & Kesselman, M. (1993) Advanced x-ray detectors for the analysis of materials. *J. Low Temp. Phys.* **93**, 779–784.
- Martinis, J.M., Nahum, M. & Castles, S. (1997) Particle calorimeter with normal metal base layer. U.S. Patent 5,634,718, issued 3 June 1997.
- McCammon, D., Cui, W., Juda, M., Morgenthaler, J. & Zhang, J. (1993) Thermal calorimeters for high resolution x-ray spectroscopy. *Nucl. Instrum. Methods Phys. Res. A*, **326**, 157–165.
- McCammon, D., Cui, W., Juda, M., Plucinsky, P., Zhang, J., Kelley, R.L., Holt, S.S., Madejski, G.M., Moseley, S.H. & Szymkowiak, A.E. (1991) Cryogenic microcalorimeters for high resolution spectroscopy: current status and future prospects. *Nucl. Phys. A*, **527**, 821c–824c.
- Mears, C.A., Labov, S.E., Frank, M., Lindeman, M.A., Hiller, L.J., Netel, H. & Barfknecht, A.T. (1996) Analysis of pulse shape from a high-resolution superconducting tunnel junction x-ray spectrometer. *Nucl. Instrum. Methods Phys. Res. A*, **370**, 53–56.
- Moseley, S.H., Mather, J.C. & McCammon, D. (1984) Thermal detectors as x-ray spectrometers. *J. Appl. Phys.* **56**, 1257–1262.
- Nahum, M. & Martinis, J.M. (1995) Hot-electron microcalorimeters as high-resolution x-ray detectors. *Appl. Phys. Lett.* **66**, 3203–3205.
- Nordfors, B. (1955) A note on the Al $K\alpha_3\alpha_4$ lines in metal and oxide. *Proc. Phys. Soc. A*, **68**, 654–656.
- Perkins, S.T., Cullen, D.E., Chen, M.H., Hubbell, J.H., Rathkopf, J. & Scofield, J. (1991) *Tables and graphs of atomic subshell and relaxation data derived from the LLNL Evaluated Atomic Data Library (EADL), Z=1–100*. Lawrence Livermore National Laboratory, Livermore, CA.
- Reed, S.J.B. (1995) Wavelength dispersive spectrometry: a review. *X-ray Spectrometry in Electron Beam Instruments* (ed. by D. B. Williams, J. I. Goldstein and D. E. Newbury), pp. 221–238. Plenum Press, New York.
- Reif, F. (1965) *Fundamentals of Statistical and Thermal Physics*, pp. 213, 242. McGraw Hill, New York.
- Schnopper, H.W. (1967) Atomic readjustment to an inner-shell vacancy: Manganese K x-ray emission spectra from an Fe^{55} K-

- capture source and from the bulk metal. *Phys. Rev.* **154**, 118–123.
- SEMATECH (1995) *Particle Composition Analysis Metrology Roadmap – A Supplement to the National Technology Roadmap for Semiconductors*. Semiconductor Industry Association, San Jose, CA.
- Silver, E., LeGros, M., Austin, G., Madden, N., Beeman, J. & Haller, E. (1997) The first use of NTD germanium-based microcalorimeters for high resolution, broad band x-ray microanalysis. *X-Ray Spectrom.*, in press.
- Silver, E., LeGros, M., Madden, N., Beeman, J. & Haller, E. (1996) High-resolution, broad-band microcalorimeters for x-ray microanalysis. *X-Ray Spectrom.* **25**, 115–122.
- Skocpol, W.J., Beasley, M.R. & Tinkham, M. (1974) Phase-slip centers and nonequilibrium processes in superconducting tin microbridges. *J. Low Temp. Phys.* **16**, 145–167.
- Statham, P. (1995) Quantifying benefits of resolution and count rate in EDX microanalysis. *X-ray Spectrometry in Electron Beam Instruments* (ed. by D. B. Williams, J. I. Goldstein and D. E. Newbury), pp. 101–126. Plenum Press, New York.
- Tinkham, M. (1980) *Introduction to Superconductivity*. McGraw-Hill, New York.
- Welty, R.P. & Martinis, J.M. (1991) A series array of DC SQUIDS. *IEEE Trans. Mag.* **27**, 2924–2926.
- Wollman, D.A., Hilton, G.C., Irwin, K.D., Dulcie, L.L., Newbury, D.E. & Martinis, J.M. (1997a) High-energy-resolution microcalorimeter spectrometer for EDS x-ray microanalysis. *Proc. Microsc. Microanalysis* (ed. by G. W. Bailey, R. V. W. Dimlich, K. B. Alexander, J. J. McCarthy and T. P. Pretlow). Springer, New York, in press.
- Wollman, D.A., Hilton, G.C., Irwin, K.D. & Martinis, J.M. (1996) EDS x-ray microcalorimeters with 13 eV energy resolution. *Proc. Microsc. Microanal.* 1996 (ed. by G. W. Bailey, J. M. Corbett, R. V. W. Dimlich, J. R. Michael and N. J. Zaluzec), pp. 488–489. San Francisco Press, San Francisco.
- Wollman, D.A., Jezewski, C., Hilton, G.C., Xiao, Q.-F., Irwin, K.D., Dulcie, L.L. & Martinis, J.M. (1997b) Use of polycapillary optics to increase the effective area of microcalorimeter spectrometers. *Proc. Microsc. Microanalysis* (ed. by G. W. Bailey, R. V. W. Dimlich, K. B. Alexander, J. J. McCarthy and T. P. Pretlow). Springer, New York, in press.